

Volume 2, Issue I

ISSN: 3021-9795 (Print)  
ISSN: 3059-9628 (Online)  
February 2025

## POKHARA ENGINEERING COLLEGE JOURNAL (PECJ)

*Applied Sciences and Engineering Insights*

"A double-blind, peer-reviewed, open-access journal indexed  
in NepJOL, dedicated to advancing knowledge  
and research dissemination."



### **Pokhara Engineering College (PEC)**

Phirke, Pokhara-8, Kaski, Nepal  
PO Box: 540, Tel: 977-61-581209/578530  
E-mail: [info@pec.edu.np](mailto:info@pec.edu.np)  
[www.pec.edu.np](http://www.pec.edu.np)

## About the Journal

### Focus and Scope

Pokhara Engineering College Journal (PECJ) is a scientific journal published by Pokhara Engineering College (PEC). PECJ covers a broad spectrum of applied sciences and engineering topics.

Our aim is to be a high-quality, multi-disciplinary journal publishing the results of basic and applied research. We place emphasis on the quality of all published papers. The journal should also bridge basic research in natural sciences and applied research in all technical disciplines.

We support the innovative research results published by young scientists or doctoral fellows and the high-quality papers by researchers from the international scientific community.

### Peer Review Process

The Editorial Board assesses all papers, and accepted papers are reviewed by at least two independent reviewers in a **double-blind review process**.

**The review process is usually completed within four months.**

### Open Access Policy

PEC Journal is an Open Access journal, meaning that all content is freely available to the user or his/her institution without charge. Users are allowed to read, download, copy, distribute, print, search, or link to the full texts of the articles in this journal without asking prior permission from the publisher or the author.

Article submission or **processing charge** (APC, publication fee) is not required from authors - publishing in PECJ is **free**.

### Periodicity

Annually.

### Copyright Policy

Pokhara Engineering College Journal (ISSN: 3021-9795). Copyright © 2025 Pokhara Engineering College. Published by Pokhara Engineering College and distributed under the terms of the Creative Commons Attribution-Non-commercial 4.0 International License (CC BY-NC 4.0), permitting use, distribution, and reproduction in any medium for non-commercial purposes, provided the original work is properly cited.



# Editorial Team

## **Advisors**

Dr. Ganesh Man Gurung  
Professor and Chancellor, Gandaki University

Dr. Dericks Praise Shukla  
Professor, IIT Mandi

Dr. Govind Prasad Lamichhane  
Professor, School of Engineering, Pokhara University

Dr. Madhab Prasad Koirala  
Professor, School of Engineering, Pokhara University

## **Editor-in-Chief**

Dr. Abhishek Ghimire  
Assistant Professor, Pokhara Engineering College

## **Managing Editor**

Er. Krishna Ghimire  
Assistant Professor, Pokhara Engineering College

## **Editor**

Dr. Rajib Raj Pokharel  
Associate Professor, School of Engineering, Pokhara University

Dr. Prakash Devkota  
Assistant Professor, Oxford Engineering College

Dr. Niraj KC  
Assistant Professor, Western Regional Campus, Pokhara

Er. Som Gurung  
Assistant Professor, Pokhara Engineering College

Er. Yam Bahadur Thapa  
Assistant Professor, Pokhara Engineering College

Er. Suraj Basanta Tulachan  
Assistant Professor, Pokhara Engineering College

Er. Bimal Bhandari  
Assistant Professor, Pokhara Engineering College

Ar. Luna Thapa  
Assistant Professor, Pokhara Engineering College

Ar. Roshni Subedi  
Assistant Professor, Pokhara Engineering College

## TABLE OF CONTENTS

Topic	Page
Welded Connections in Structural Engineering: A Comparative Study of Design Standards	1
Study on Air Pollution and Its Dispersion Pattern in Pokhara Valley	11
Assessment of Structural Rebar Wastage of Reinforced Cement Concrete Buildings: A Case Study of School Building Type Designs in Kathmandu	23
Compliance Status of Nepal National Building Code (NBC: 105) within Pokhara Metropolitan City	38
Diabetic Retinopathy Detection through Multiclass Classification of Fundus Image Using Convolutional Neural Network	47

## Welded Connections in Structural Engineering: A Comparative Study of Design Standards

Abhishek Ghimire

Department of Civil Engineering, Pokhara Engineering College, Pokhara, Nepal

Corresponding email: [abhi.ghimire45@gmail.com](mailto:abhi.ghimire45@gmail.com)



Pokhara Engineering College Journal (ISSN: 3021-9795), Copyright © [2025] The Author(s). Published by Pokhara Engineering College, distributed under the terms of the Creative Commons Attribution 4.0 International License (CC BY-NC 4.0).

Received: 20-November-2024; Revised: 19-January-2025; Accepted: 20-January-202

### Abstract

This paper comprehensively reviews analytical approaches for designing welded connections based on established design standards, including European, US, and Indian standards. The study emphasizes the behaviour of fillet welds under various load directions, demonstrating that their strength depends significantly on the orientation of the applied forces. Through detailed analysis of design guidelines and independent research, this review highlights the directional and mean stress methods in European standards, the Load and Resistance Factor Design (LRFD) and Allowable Stress Design (ASD) in US standards and Indian standards. The findings offer a comparative perspective on welded connections' load-bearing capacity and resistance factors, providing valuable insights such as guidance on selecting standards based on loading conditions and material strength considerations for safer and cost-effective welded connections.

**Keywords:** Fillet welds, Filler metal, Base metal, Load bearing capacity, weld direction

### 1. Introduction

Welding is the process of assembling two or more metallic parts by fusing them and filling them in with molten metal from the electrode (Bernuzzi and Cordova, 2016). Structural integrity is one of the important aspects in many industrial sectors where welding is a primary technique for connection (Ghimire *et al.*, 2024; Ghimire *et al.*, 2024). Many steel industries are working to develop light and slender constructions of steel structures having good welding characteristics and high ductility (Spiegler, 2018). Weld materials are referred to as the material which is added to the joint in its liquid state while necessary to connect the base material during the welding process. There are two types of welding process, autogenous process (base metal participates in the formation of the joint by fusion or crystallization with the weld metal if present) and heterogeneous process (only the base material is the weld material used at a temperature lower than the melting temperature of the base material) (Bernuzzi and Cordova, 2016). It is essential to ensure the strength, ductility, and toughness of welded connections to allow for the redistribution of stresses and internal forces when using steel (Günther *et al.*, 2012). Failures in welded connections can lead to catastrophic structural collapses, causing financial losses and endangering lives.

In construction, various types of welded connections are used, including fillet welds, all-around fillet welds, butt welds, plug welds, and flare groove welds. The selection of each type depends

on its specific properties (European Committee for Standardization (CEN), 2005). Fillet welds and partial penetration connections are widely utilized in building construction due to their practicality and versatility. Design engineers often prefer fillet welds over other connection types, primarily because of compliance with standards, technical constraints, and the economic efficiency of welding materials. Consequently, the design of fillet welds must not only meet the strength requirements specified in design codes but also ensure cost-effectiveness (Taheri *et al.*, 2024). Extensive experimental and analytical research has been conducted to examine the behaviour of fillet welds and accurately predict their strength and ductility (Kanvinde *et al.*, 2009).

Designing welded connections requires adherence to stringent standards and guidelines established by various international codes. Eurocode, American Welding Society (AWS), and Indian standards were chosen for their global usage and varying design philosophies, providing a comprehensive basis for comparison. However, significant variations exist in the methodologies prescribed by these standards, particularly regarding the evaluation of fillet weld strength and the effects of directional loading.

This paper aims to provide a detailed comparative analysis of the approaches recommended by these codes. It focuses on critical aspects such as the influence of weld orientation on strength, the role of filler and base metals in resisting loads, and the design philosophies underpinning methods like directional and mean stress analysis, Load and Resistance Factor Design (LRFD), and Allowable Stress Design (ASD). By synthesizing insights from diverse design standards, this review seeks to guide engineers in selecting optimal design strategies for welded connections that balance safety, efficiency, and material economy.

## 2. Standards for Fillet Welded Connections

### 2.1 European Standards

The structural performance of the welded connection depends on the joint type and the corresponding load situation. According to Eurocode EN 1993-1-8 (European Committee for Standardization (CEN), 2005) and EN 1993-1-12 (European Committee for Standardization (CEN), 2011), the design strength of fillet welded connection is calculated from two different methods; the directional method and the mean stress method.

#### 2.1.1 Directional Method

For a more accurate directional method, the forces transmitted by the weld are resolved into stress components  $\sigma_{\perp}$ ,  $\tau_{\perp}$ , and  $\tau_{\parallel}$  within the area of the throat section because it is assumed to form the resisting and failing section (Kuhlmann *et al.*, 2008). The design resistance of the fillet welded connection is expressed in equation 1 as a function of the tensile strength of the base material along with the correlation factor  $\beta_w$ . However, the strength of the filler metal is not considered. According to EN 1993-1-8 (European Committee for Standardization (CEN), 2005), the normal stress parallel to the weld axis is not considered when verifying the design resistance of the weld. The resolved stress components  $\sigma_{\perp}$ ,  $\tau_{\perp}$ , and  $\tau_{\parallel}$  helps to optimize weld design are shown in Figure 1 are calculated from design loads with the assumption of uniform stress distribution in the weld throat. The methodology is based on the description of an ultimate strength surface expressed by the Huber-Hencky-von-Mises criterion resulting in an equivalent stress  $\sigma_{w,Ed}$  (Kuhlmann *et al.*, 2008).

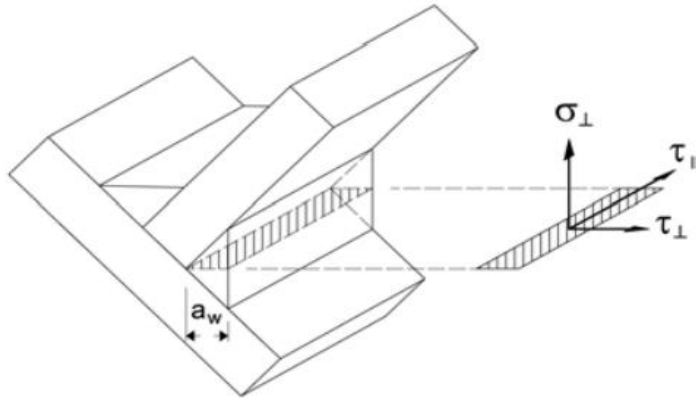


**Figure 1:** Stress Components longitudinal and perpendicular to the weld throat (Günther *et al.*, 2009).

$$\sigma_{w,Ed} = \sqrt{\sigma_{\perp}^2 + 3\tau_{\perp}^2 + 3\tau_{\parallel}^2} \leq \frac{f_u}{\beta_w \times \gamma_{M2}} \text{ and } \sigma_{\perp} \leq \frac{0.9 \times f_u}{\gamma_{M2}} \quad (1)$$

where  $\sigma_{\perp}$  is the normal stress perpendicular to the throat,  $\tau_{\perp}$  is the shear stress perpendicular to the axis of the weld,  $\tau_{\parallel}$  is the shear stress parallel to the axis of the weld,  $f_u$  is the tensile strength of the base metal (Weaker part of the joined base metals),  $\gamma_{M2}=1.25$  is the partial safety factor for the resistance of welds, and  $\beta_w$  is the correlation factor depends on the grade of steel which is increased from 0.8 for mild steel to 1.0 for high strength steel see in Table 1 (European Committee for Standardization (CEN), 2005) and (European Committee for Standardization (CEN), 2011).

**Table 1:** Correlation factor  $\beta_w$  depending on standard and steel grade (European Committee for Standardization (CEN), 2005).

Standard and steel grade			Correlation factor
EN 10025	EN 10210	EN 10219	$\beta_w$
S235	S235 H	S235 H	0.8
S235 W			
S275	S275 H	S275 H	0.85
S275 N/NL	S275 NH/NLH	S275 NH/NLH	
S275 M/ML		S275 MH/MLH	
S355		S355 H	0.9
S355 N/NL	S355 H	S355 NH/NLH	
S355 M/ML	S355 NH/NLH	S355 MH/MLH	
S355 W			
S420 N/NL		S420 MH/MLH	1.0
S420 M/ML			
S460 N/NL			1.0
S460 M/ML	S460 NH/NLH	S460 NH/NLH	
S460 Q/QL/QL1		S460 MH/MLH	



### 2.1.2 Simplified Method

The mean stress method is a simplification of the directional method. The design resistance of a fillet weld may be assumed to be adequate if, at every point along its length the resultant of all forces per unit length transmitted by the weld  $F_{w,Ed}$  satisfy the following criteria:

$$F_{w,Ed} \leq F_{w,Rd}$$

Where  $F_{w,Ed}$  is the design value of the weld force per unit length and  $F_{w,Rd}$  is the design weld resistance per unit length.

The design weld resistance per unit of weld should be determined using equation 2, regardless of the orientation of the weld throat plane to its applied force (European Committee for Standardization (CEN), 2005).

$$F_{w,Rd} = f_{vw,d} \times a \quad (2)$$

$$f_{vw,d} = \frac{f_u}{\sqrt{3} \beta_w \gamma_{M2}}$$

Where  $f_{vw,d}$  is the design shear strength of the weld and  $a$  is the effective throat thickness of the fillet weld which should be taken as the height of the largest triangle (with equal or unequal legs) that can be inscribed within the fusion faces and the weld surface, measured perpendicular to the outer side of this triangle and should not be less than 3 mm as per clause 4.5.2 (1) and (2) (European Committee for Standardization (CEN), 2005).

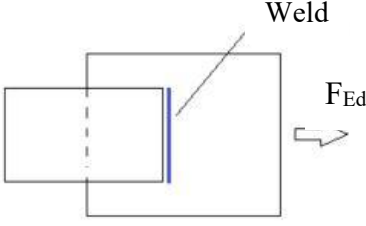
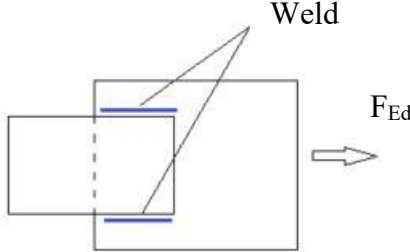
**Table 2:** Values for the design weld resistance according to EN 1993 in case of fillet welds,  $t \leq 40$  mm (Günther *et al.*, 2009).

Steel grade		S235	S355	S460	S690
$f_y$	[MPa]	235	355	460	690
$f_u$	[MPa]	360	510	540	770
$\beta_w$		0.8	0.9	1.0	1.0
$\frac{f_u/\sqrt{3}}{\beta_w \gamma_{M2}}$	[MPa]	360	453	432	616

The design weld resistance for welds is outlined in the standards EN 1993-1-1 (European Committee for Standardization, 2010), EN 1993-1-8 (European Committee for Standardization (CEN), 2005), and EN 1993-1-12 (European Committee for Standardization (CEN), 2011). This resistance varies based on structural steel grades as specified in EN 10025-2 (European Committee for Standardization, 2004), EN 10025-3 (British Standards, 2004), and EN 10025-6 (European Committee for Standardization, 2004). For fillet welds with a thickness of  $t \leq 40$  mm, the information is summarized in Table 2. The table illustrates that the design resistance of the higher-strength steel grade S460 is somewhat lower than that of the steel grade S355.

Example calculations for welds perpendicular and parallel to the direction of an applied force, along with the design resistance of fillet welds according to European Standards, are presented in Tables 3 and 4.

**Table 3:** Design resistance of welds perpendicular and parallel to the direction of action of force according to Eurocode (European Committee for Standardization (CEN), 2005).

Sample	Description	Details
	Normal and Shear stress perpendicular to the direction of force:	$\sigma_{\perp} = \tau_{\perp} = \frac{F_{Ed}}{\sqrt{2} A_w}$
	Directional Method	$\sqrt{\sigma_{\perp}^2 + 3\tau_{\perp}^2} \leq \frac{f_u}{\beta_w \gamma_{M2}}$
	Simplified Method	$\frac{F_{Ed}}{A_w} \leq \frac{f_u}{\sqrt{2} \cdot \beta_w \gamma_{M2}}$
	Comparison	Directional Method gives 22% more durable results than that of simplified method.
	Shear stress parallel to the direction of force:	$\tau_{\parallel} = \frac{F_{Ed}}{A_w}$
	Directional Method	$\sqrt{3\tau_{\parallel}^2} \leq \frac{f_u}{\beta_w \gamma_{M2}}$
	Simplified Method	$\frac{F_{Ed}}{A_w} \leq \frac{f_u}{\sqrt{3} \cdot \beta_w \gamma_{M2}}$
	Comparison	Same strength from both method

**Table 4:** Design resistance of fillet welds according to EN 1993-1-8 (European Committee for Standardization (CEN), 2005).

	Combination of base metal & filler metal	
	S690Q-G42	S690-G46
Base Metal ( $f_y$ ) [N/mm <sup>2</sup> ]	690	690
Base Metal ( $f_u$ ) [N/mm <sup>2</sup> ]	770	770
Filler Metal ( $f_y$ ) [N/mm <sup>2</sup> ]	420	460
Filler Metal ( $f_u$ ) [N/mm <sup>2</sup> ]	500	530
$\beta_w$	1	1
$\gamma_{M2}$	1.25	1.25
$f_{vw,d} = \frac{f_u/\sqrt{3}}{\beta_w \gamma_{M2}}$	230.94	244.80

## 2.2 US Standards

In the US, load and resistance factor design (LRFD) and allowable strength design (ASD) methods are considered for the design strength of weld according to ANSI/AISC 360-16 (American Institute of Steel Construction, 2016). Fillet welds are often considered the weakest component due to their geometry, which concentrates stresses at critical points, leading to potential failures under high loads. The design strength of the fillet weld is determined using section J2.4 in ANSI/AISC 360-16 (American Institute of Steel Construction, 2016). According to ANSI/AISC 360-16 (American Institute of Steel Construction, 2016), the directional strength of fillet welds loaded perpendicular to the weld axis is increased by 50%.

The design strength  $\phi R_n$  of welded joints shall be the lower of the base material strength and the weld metal strength. The weld metal strength is determined according to the limit state of rupture, and base material strength is determined according to the limit states of tensile rupture and shear rupture as follows:

For the base metal. However, the base metal check is not required for matching electrodes.

$$\phi R_n = \phi F_{nBM} A_{BM} \quad (3)$$

For the filler metal

$$\phi R_n = \phi F_{nw} A_{we} \quad (4)$$

Where  $A_{BM}$  is the base metal's cross-sectional area,  $A_{we}$  is the weld's effective area,  $F_{nBM}$  is the nominal stress of the base metal, and  $F_{nw}$  is the nominal stress of the weld metal. The values of  $\phi$ ,  $\Omega$ , and  $F_w$  and limitations thereon, are given in Table J2.5 of ANSI/AISC 360-16 (American Institute of Steel Construction, 2016).

The design strength for a linear weld group through the centre of gravity having a uniform leg size is determined as follows:

$$\phi R_n = \phi 0.60 F_{EXX} (1.0 + 0.50 \sin^{1.5}(\theta)) A_{we} \quad (5)$$

Where  $F_{EXX}$  is the filler metal classification strength, and  $\theta$  is the angle between the direction of the force and the weld axis.

The load-bearing capacity of a welded connection is determined based on the type of filler metal used. Specifying the steels associated with the filler metals is important to make effective comparisons with other standards. Table 5.3 of AWS D1.1/D1.1M:2020 (American Welding Society, 1980) provides a selection of potential steel and welding consumables combinations. Some strengths of steels and their associated welding consumables are listed in Table 5, along with the design weld strength presented in Table 6.

**Table 5:** Strength of steels with associated welding consumables according to AISC 360-16 (American Institute of Steel Construction, 2016)(AWS D1.1/D1.1M:2020) (American Welding Society, 1980).

Steel	$f_y$ [N/mm <sup>2</sup> ]	$f_u$ [N/mm <sup>2</sup> ]	$F_{EXX}$
A36 ( $\leq 20$ mm)	250	400-550	60 ksi/70 ksi (414/483 N/mm <sup>2</sup> )
A913 (Size 50)	345	Min. 455	70 ksi (483 N/mm <sup>2</sup> )
A913 (Size 60)	415	Min. 520	80 ksi (552 N/mm <sup>2</sup> )
A913 (Size 65)	450	Min. 550	80 ksi (552 N/mm <sup>2</sup> )
A852	485	620-760	90 ksi (621 N/mm <sup>2</sup> )

**Table 6:** Design strength of fillet welds according to AISC 360-16 (American Institute of Steel Construction, 2016), [AWS D1.1, 2020] (American Welding Society, 1980).

	Welding Consumables material		
	60 ksi	70 ksi	80 ksi
$f_y$ [ksi/ N/mm2]	48/331	57/393	67/462
$f_u$ [ksi/ N/mm2]	60/414	70/483	80/552
$F_{EXX}$ [N/mm2]	414	483	552
$\emptyset$ [-]		0.75	
$\emptyset * 0.60 * F_{EXX}$	186.3	217.35	248.4
$\emptyset * 0.60 * F_{EXX} (1.0 + 0.50 * \sin^{1.5}(\theta))$			
$\theta = 0^\circ$ (welds parallel to the direction of force)	186.3	217.35	248.4
$\theta = 90^\circ$ (welds perpendicular to the direction of force)	279.45	326.03	372.6

### 2.3 Indian Standards

The design shear strength of the fillet welded connection as per Indian standards IS 800-2007 (BIS (Bureau of Indian Standards), 2007) is given in the equation (6).

$$V_{dw} = \frac{f_u}{\sqrt{3}\gamma_{mw}} \times L_w \times t_e \quad (6)$$

Where  $f_u$  is the ultimate strength of the weld or parent metal, whichever is minimum,  $L_w$  is the effective length of the weld,  $t_e$  is the effective throat thickness of the weld, and  $\gamma_{mw}$  is the partial safety factor. Table 7 illustrates the design of resistance welds with different welding combinations.

According to IS 800-2007 (BIS (Bureau of Indian Standards), 2007), the size of fillet welds must not be less than 3 mm. To prevent the risk of cracking without preheating, the minimum size of the first run or a single-run fillet weld is specified in Table 21 of IS 800-2007 (BIS (Bureau of Indian Standards), 2007). In practice, the actual length of the weld should be the effective length plus two times the size of the weld, but it must not be less than four times the size of the weld. Additionally, the effective throat thickness of a fillet weld should be no less than 3 mm and, generally, should not exceed  $0.7t$  or  $1.0t$  under exceptional circumstances, where ' $t$ ' is the thickness of the thinner plate being welded.

**Table 7:** Design resistance of fillet welds according to IS 800-2007 (BIS (Bureau of Indian Standards), 2007).

	Welding combination		
	Combination-I	Combination-II	Combination-III
Base Plate ( $f_u$ ) [N/mm2]	410	360	490
Filler Metal ( $f_u$ ) [N/mm2]	490	490	490
$\gamma_{mw}$	1.25	1.25	1.25
$V_{dw} = \frac{f_u/\sqrt{3}}{\gamma_{mw}}$	189.37	166.27	226.32

### 3. Comparison of strength for fillet welded connection

Using a specific example, this section compares the design strength for fillet welded connections based on the aforementioned standards. The parent and filler materials are assumed to have an ultimate tensile strength of 360 MPa. This example considers a weld with a throat thickness of 3 mm and a length of 100 mm. The strength of the fillet welded connection is evaluated for two loading directions: parallel and perpendicular to the weld. The comparative design resistances, calculated according to European, US, and Indian standards, are presented in Table 9.

**Table 9:** A comparison of the design strength of fillet welded connections based on different standards.

Standards	The direction of the line of action		
	Parallel to the weld	Perpendicular to the weld	Perpendicular/Parallel
European Standard	62.35 kN	76.37 kN	1.22
US Standard	48.60 kN	72.9 kN	1.50
Indian Standard	49.88 kN	61.01 kN	1.22

The results presented in Table 9 reveal significant variations in the predicted design strength of fillet welded connections based on different international standards. These differences can be attributed to each standard's distinct methodologies, safety factors, and material strength considerations. In addition to this, Variations in predicted design strength across standards influence material selection, construction costs, and safety. For instance, a more conservative standard might require additional material, impacting cost but enhancing safety margins.

- European Standard: The design resistance predicted by the European Standard is higher when the load is perpendicular to the weld (76.37 kN) compared to parallel loading (62.35 kN). This indicates a more conservative approach in estimating resistance for parallel loading, with a perpendicular-to-parallel strength ratio of 1.22.
- US Standard: The US Standard shows a relatively balanced prediction, with a higher resistance under perpendicular loading (72.90 kN) and a lower resistance under parallel loading (48.60 kN). Notably, the perpendicular-to-parallel ratio of 1.50 is the highest among the standards, suggesting a more pronounced difference in strength predictions between the two loading directions.
- Indian Standard: The Indian Standard also reflects higher resistance under perpendicular loading (61.01 kN) compared to parallel loading (49.88 kN), with a perpendicular-to-parallel ratio of 1.22, similar to the European Standard. This suggests alignment in their design philosophy regarding directional strength variations.

The comparison highlights that all three standards consistently predict higher strength for perpendicular loading than for parallel loading. This aligns with the physical behavior of fillet welds, where the weld's capacity is generally greater under perpendicular loading due to the orientation of stress distribution and weld geometry.

However, the US Standard predicts a much more significant disparity between the two loading directions than the European and Indian Standards. This could indicate a more conservative approach in accounting for uncertainties in parallel loading scenarios or differing assumptions about stress transfer mechanisms. The conservative nature of the US standard prioritizes safety but may lead to overdesign in certain scenarios.

These differences underscore the importance of understanding the underlying assumptions and safety margins of each standard. For design engineers, this comparison emphasizes the need to select appropriate standards based on the specific application, ensuring that the design aligns with both safety and performance requirements.

#### 4. Summary

This study has reviewed and compared analytical methods for designing welded connections across various international standards, highlighting similarities and differences in approaches. The study reveals Eurocode's directional method yields higher resistance for perpendicular loading, while the US standard adopts a more conservative approach, leading to safer but potentially overdesigned connections. Highlighting these differences provides clear guidance for material and method selection in structural applications.

Overall, the analysis underscores the importance of selecting appropriate design methodologies based on project-specific requirements, material properties, and local standards. Insights from this study can enhance engineering education by integrating cross-standard comparisons into curricula and assist practitioners in adapting codes for local construction challenges, ensuring optimal performance and safety.

#### References

American Institute of Steel Construction (2016) *AISC360/16 Specification for Structural Steel Buildings*, an American National Standard, pp. 1–612.

American Welding Society (1980) *AWS D1.1/D1.1M:2020 An American National Standard, Structural Welding Code-Steel*. American National Standards Institute, Standards.

Bernuzzi, C. and Cordova, B., 2016. *Structural steel design to Eurocode 3 and AISC specifications*. John Wiley & Sons.

BIS (Bureau of Indian Standards) (2007) *IS 800:2007 General Construction In Steel-Code Of Practice*. New Delhi.

British Standards (2004) *Hot rolled products of structural steels— Part 3: Technical delivery conditions for normalized/normalized rolled weldable fine grain structural steels*. BS EN 10025-3:2004. Available at: <https://bsol.bsigroup.com/en/Bsol-Item-Detail-Page/?pid=000000000030157914>.

European Committee for Standardization (2004) *BS EN 10025-2: Hot rolled products of structural steels-Part 2: Technical delivery conditions for non-alloy structural steels*. Available at: [https://members.marticonet.sk/jkuba/normy/EN\\_10025-2-2004\\_BS\\_HotRolledProduct\\_TDCforNonAlloySteels.pdf](https://members.marticonet.sk/jkuba/normy/EN_10025-2-2004_BS_HotRolledProduct_TDCforNonAlloySteels.pdf).

European Committee for Standardization (2010) *Eurocode 3: Part 1-1: General rules and rules for buildings*. Available at: <http://doi.wiley.com/10.1002/9783433601099>.

European Committee for Standardization (2004) *BS EN10025-6: Hot rolled products of structural steels-Part 6: Technical delivery conditions for flat products of high yield strength structural steels in the quenched and tempered condition*.

European Committee for Standardization (CEN) (2005) *Eurocode 3: Design of steel structures — Part 1-8: Design of joints*. European Standards, CEN, 50, p. 77.

European Committee for Standardization (CEN) (2011) *Eurocode 3: Design of steel structures—Part 1-12* (Vol. 1, 2005).

Ghimire, A., Wald, F., Vild, M. and Kabeláč, J., 2024. Numerical design calculation of the fillet weld resistance. *Welding in the World*, 68(2), pp.441-458.

Ghimire, A., Wald, F., Vild, M. and Kabeláč, J., 2024. Numerical design calculation of the high-strength steel welds. *Engineering Structures*, 300, p.117201.

Günther, H.P., Hildebrand, J., Rasche, C., Christian, V., Wudtke, I., Kuhlmann, U., Vormwald, M. and Werner, F., 2012. Welded connections of high-strength steels for the building industry. *Welding in the World*, 56, pp.86-106.

Kanvinde, A.M., Gomez, I.R., Roberts, M., Fell, B.V. and Grondin, G.Y., 2009. Strength and ductility of fillet welds with transverse root notch. *Journal of Constructional Steel Research*, 65(4), pp.948-958.

Kuhlmann, U., Günther, H.P. and Rasche, C., 2008. High-strength steel fillet welded connections. *Steel Construction: Design and Research*, 1(1), pp.77-84.

Rasche, C. and Kuhlmann, U., 2012. Zur Bestimmung der Tragfähigkeit von Kehlnahtverbindungen höherfester Baustähle. *Stahlbau*, 81(11), pp.889-897.

Spiegler, J. and Kuhlmann, U., 2018. Innovative high-strength steel construction using mixed connections. *Steel Construction*, 11(4), pp.272-277.

Taheri, H., Karpenko, M., Clifton, G.C., Ramhormozian, S., Dong, P., Lim, J.B., Roy, K. and Fang, Z., 2024. Comparison between weld sizing methods included in steel structure standards.



## Study on Air Pollution and Its Dispersion Pattern in Pokhara Valley

Rajib Pokhrel<sup>1\*</sup>

*School of Engineering, Faculty of Science and Technology, Pokhara University, Nepal*

Corresponding email: [rajibp@pu.edu.np](mailto:rajibp@pu.edu.np)



Pokhara Engineering College Journal (ISSN: 3021-9795), Copyright © [2025] The Author(s). Published by Pokhara Engineering College, distributed under the terms of the Creative Commons Attribution 4.0 International License (CC BY-NC 4.0).

*Received: 29-December-2024; Revised: 26-January-2025; Accepted: 30-January-2025*

### Abstract

Regional International Airport has been in operation in the mid of Pokhara Metropolitan City where most of the farming land has been converted to the built-up area. Distinct temperature difference has been felt in between downtown and nearby sub-urban area. This study was conducted to investigate the wind flow pattern and air pollution dispersion mechanism in Pokhara. A numerical simulation technique such as A2C flow / A2C t & d was introduced to simulate the local wind flow vectors and air pollution (puffs) dispersion by locally generated

wind in the study domain. The simulation results for the study domain revealed that the air flows from the mountain region to the valley from the mid-night to the early morning around 8 AM. As the mountain region get heated after the sunshine, the flow velocity decreases and reaches to the transition state around 09:00 – 10:00 AM. Then flow direction changes towards the mountain region after 11 AM and the velocity reaches the maximum around 2 PM to 3 PM. It is continuous till mid-night around 9 PM to 10 PM and again reaches to the transition period. The locally generated wind plays significant role for the transport and dispersion of air pollution (puff) generated from the source to the surrounding region. Generally, urban air pollution generated in the valley area accumulated in the valley region in the mid-night to the early morning and it disperses around the upper air mostly above the mountain region. Mostly, the pollution generated nearby the mountain region disperses above the mountain region in the daytime. Hence it is concluded that the pollution generated from the difference sources such as aviation, automobiles, industries and the construction sites in the periphery of Pokhara Metropolitan City disperses around the Valley and reached up to the nearby mountain region.

**Keywords:** *Air Pollution, Air Dispersion, Meteorology, Numerical Simulation*

### 1. Introduction

Construction activities, automobiles have been notably increasing in Pokhara with the increase of population. Its natural beauty has been deteriorating day by day due to the increased pollution as well as haphazard urbanization. Recently, numbers of road development, residential / commercial building construction activities, construction and operation of mega projects such as Pokhara International Airport, Prithvi Highway, number of industries, etc. have been in operation stage in Pokhara which noticeably impacted the air quality of the Valley. In general, construction practice in Nepal is open, while air emissions such as Particulate Matters (PM), gaseous emissions, etc. easily disperse in the atmospheric environment.





**Figure 1.** Major sources of air pollution in Pokhara; (a) Stack emission from the Industrial area and (b) dust dispersion in the construction site during the construction stage.

A mega project, new international airport was in construction phase since 13 April 2016 in the centre of Pokhara Metropolitan City and it has already been in operation where particulate emission deteriorates the visibility around the Pokhara as in Fig. 1(b). Earth moving operations is the most important contributor of PM emissions across the construction industry where truck loading and dumping of crushed rocks and mud, and dirt carryout from construction site to the destination via adjoining roads are major sources of PM emission. Moreover, most of the industries operated in Pokhara Industrial Estate emitted the air pollution as in Fig. 1(a) which may noticeably contributed the particulate as well as gaseous pollutant in the surrounding area.

There are three real time air quality monitoring station in Pokhara Valley at (a) Gandaki Boarding School, (b) DHM Pokhara and (c) Pokhara University. Some stations data have been updated at the website for public information but cannot download the detail data for research and analysis purpose. There was not a real time air quality monitoring system near the airport construction area therefore it is difficult to identify how much the air pollution was added from the airport construction activity in Pokhara valley and its effective zone around Pokhara. Moreover, approximately 200 ha of firm land has been converted to concrete and constructed land as Pokhara International Airport in the heart of Pokhara. In the recent decade, the land use pattern in the Pokhara Valley noticeably changed to the built-up area as an Airport, residential and commercial area which may affect the local meteorology and air dispersion mechanism too. Lana et al. reported that the stable meteorological condition overshadowed the air pollution level in the city (Laña et al., 2016). Wind influences the dispersion of air pollutants. Strong winds can dilute pollutant concentrations by dispersing them over a larger area, while stagnant conditions (low wind speed) can lead to the accumulation of pollutants. The direction of the wind also determines where pollutants are transported, potentially affecting regions far from their source (Jacob, 1999). In urban area, most of the land is covered with civil structures, consequently the urban areas experience unique meteorological conditions due to the urban heat island (UHI) effect, which exacerbates pollutant concentrations (Wond and Chen, 2009). Therefore, numerical simulation techniques such as Lagrangian approach (A2C model) has been introduced in this research to understand the air dispersion pattern and estimate air pollution dispersion zone in the Pokhara valley. A2C model has already been widely used for such study around the world as it is built up with effective numerical approach in simple operating procedure which takes less time and space for the simulation (Pokhrel and Lee, 2011; Pokhrel and Ghimire, 2020).

## 2. Air Dispersion Modelling

Modeling technique is an essential tool for atmospheric environmental studies together with observational data. Models are based upon semi-empirical statistical relations among available data and measurements. This study introduced the air dispersion in the study area using computer modelling based on the Lagrangian Approach. A2C (Atmospheric to Computational fluid dynamics) flow and A2C t&d (transport & diffusion) are the updated versions of HOTMAC and RAPTAD, respectively. The basic equations of HOTMAC for mean wind, temperature, mixing ratio of water vapour, and turbulence are similar to those used by Yamada (1981, 1985). It has the addition of nested grid capability and the effect of shadows produced by the terrain. The terrain vertical coordinate system is used in this model in order to increase the accuracy in the treatment of surface boundary conditions.

$$z^* = \bar{H} \frac{z - z_g}{H - z_g} \quad (1)$$

Where  $z^*$  and  $z$  are the transformed and Cartesian-vertical coordinates, respectively;  $z_g$  is ground elevation;  $\bar{H}$ , the material surface top of the model in the  $z^*$  coordinate; and  $H$ , the corresponding height in the  $z$  - coordinate. The governing equations following the coordinate transformation based on Yamada (1981) (Yamada, 1981) are

$$\frac{DU}{Dt} = f(V - V_g) + g \frac{\bar{H} - z^*}{\bar{H}} \left( 1 - \frac{\langle \theta_v \rangle}{\theta_v} \right) \frac{\partial z_g}{\partial x} + \frac{\partial}{\partial x} \left( K_x \frac{\partial U}{\partial x} \right) + \frac{\partial}{\partial y} \left( K_{xy} \frac{\partial U}{\partial y} \right) + \frac{\bar{H}}{H - z_g} \frac{\partial}{\partial z^*} (-\overline{uw}) \quad (2)$$

$$\frac{DV}{Dt} = -f(U - U_g) + g \frac{\bar{H} - z^*}{\bar{H}} \left( 1 - \frac{\langle \theta_v \rangle}{\theta_v} \right) \frac{\partial z_g}{\partial y} + \frac{\partial}{\partial x} \left( K_{xy} \frac{\partial V}{\partial x} \right) + \frac{\partial}{\partial y} \left( K_y \frac{\partial V}{\partial y} \right) + \frac{\bar{H}}{H - z_g} \frac{\partial}{\partial z^*} (-\overline{vw}) \quad (3)$$

$$\frac{\partial U}{\partial x} + \frac{\partial V}{\partial y} + \frac{\partial W^*}{\partial z^*} - \frac{1}{H - z_g} \left( U \frac{\partial z_g}{\partial x} + V \frac{\partial z_g}{\partial y} \right) = 0 \quad (4)$$

Where,

$$W^* = \frac{\bar{H}}{H - z_g} W + \frac{z^* - \bar{H}}{H - z_g} \left( U \frac{\partial z_g}{\partial x} + V \frac{\partial z_g}{\partial y} \right) \quad (5)$$

and

$$\frac{D()}{Dt} = \frac{\partial ()}{\partial t} + U \frac{\partial ()}{\partial x} + V \frac{\partial ()}{\partial y} + W^* \frac{\partial ()}{\partial z^*} \quad (6)$$

In the above expression  $\langle \rangle$  indicates an average over a horizontal surface.  $\theta_v = ((P_0 / P)^{R/C_p} (1 + 0.61 Q_v) T)$  is the virtual potential temperature;  $f$  for coriolis parameter;  $g$  for acceleration of gravity;  $P$  for pressure;  $P_0$  for a reference pressure;  $C_p$  for specific heat capacity of dry air at constant pressure ( $= 1.003 \text{ Jg}^{-1} \text{ K}^{-1}$ );  $R$  for gas constant for dry air ( $= 0.28704 \text{ Jg}^{-1} \text{ K}^{-1}$ );  $Q_v$  for mixing ratio of water vapor;  $U$ ,  $V$ ,  $W$  for mean velocity in  $x$ ,  $y$ ,  $z$  directions, respectively;  $u$ ,  $v$ ,  $w$  for velocity fluctuations. The second term on the right-hand side of eq. (2) and eq. (3) indicate the effect of ground slope. For simplicity,  $H$  is specified as

$$H = \bar{H} + z_{g \max} \quad (7)$$

Where,  $\bar{H} = 5000 \text{ m}$  as suggested by Yamada et al. (1999) (Yamada, 1999) and  $z_{g \max}$  is generated based on topographic data. Expressions of the horizontal eddy viscosity coefficients  $K_x$ ,  $K_y$ , and  $K_{xy}$ , are referred from Yamada (1978) (Yamada, Kao and Bunker, 1989). Similarly, the equations for the computation of geostrophic winds  $U_g$  and  $V_g$  are referred from Yamada (1981) (Yamada, 1981).

Concentration distributions are assumed in different forms and one of the simplest ways is to assume a Gaussian distribution where variances are determined as the time integration of the velocity variances encountered over the history of the puff. The concentration level at a given time and place is calculated as the sum of the concentrations from each puff (Yamada, 1999). Concentration  $C$  at  $(X, Y, Z)$  is computed by using the equation (11).

$$C(X, Y, Z) = \frac{Q\Delta t}{(2\pi)^{3/2}} \sum_{k=1}^N \frac{1}{\sigma_{xk} \sigma_{yk} \sigma_{zk}} \exp\left[-\frac{1}{2} \frac{(x_k - X)^2}{\sigma_{xk}^2}\right] \times \exp\left[-\frac{1}{2} \frac{(y_k - Y)^2}{\sigma_{yk}^2}\right] \\ \times \left\{ \exp\left[-\frac{1}{2} \frac{(y_k - Y)^2}{\sigma_{yk}^2}\right] + \exp\left[-\frac{1}{2} \frac{(z_k + Z - 2z_g)^2}{\sigma_{zk}^2}\right] \right\} \quad (8)$$

Where  $(x_k, y_k, z_k)$  is the location of the  $k^{\text{th}}$  puff;  $\sigma_{xk}$ ,  $\sigma_{yk}$  and  $\sigma_{zk}$  are the standard deviations of a Gaussian distribution; and  $z_g$  is the ground elevation. Brief description of RAPTAD model was reported in detail by Yamada (Yamada, Kao and Bunker, 1989; Yamada, 2004).

### 3. Material and Method

#### 3.1. Study Site

The study site locates in Pokhara Valley which is in Gandaki Province, the Western Region of Nepal. The altitude varies from 827 meters in the southern part to 1,740 meters in the north. The Annapurna Range, with three of the ten highest mountains in the world i.e. Dhaulagiri, Annapurna I and Manaslu, are within 24 – 56 km of the valley. The valley is approximately divided into four to six parts by the rivers Seti, Bijayapur, Bagadi, Phusre and Hemja. The Seti Gandaki flowing through the city from north to south divides the city roughly in two halves. The floor of the valley is plain, resembles Terai due to its gravel-like surface, and has slanted orientation from northwest to southeast. The city is surrounded by the hills overlooking the entire valley. Out of the total area, approximately 1% of the area is covered by water. The rest of the area is covered with agricultural land, forest and built-up areas.

Millions of domestic and international tourists visit Pokhara and its vicinity every year. Shining Himalayas, pristine lakes, caves, unique culture, pleasant environment, etc., are the major beauty of Pokhara. Pokhara Regional International Airport (PRIA) is a newly constructed airport in Pokhara. It is 3 km east from the existing domestic airport, at Chinnendanda. PRIA has one runway measuring 2,500 m length and 45 m width. The airport has concrete runway, parking bays will be able to handle up to five narrow-body aircraft. Two terminals, one

domestic and one international, will be able to handle one million passengers annually. Figure 2 shows the location of PRIA in Pokhara Valley. The study domain in this study covers the whole valley area and its surrounding area which may be affected by the pollution generated in the valley area mostly from PRIA site and its periphery. Meteorological data required for setting the initial and boundary condition of the numerical simulation study are utilized from the secondary source data of nearby station as well as from the published articles.

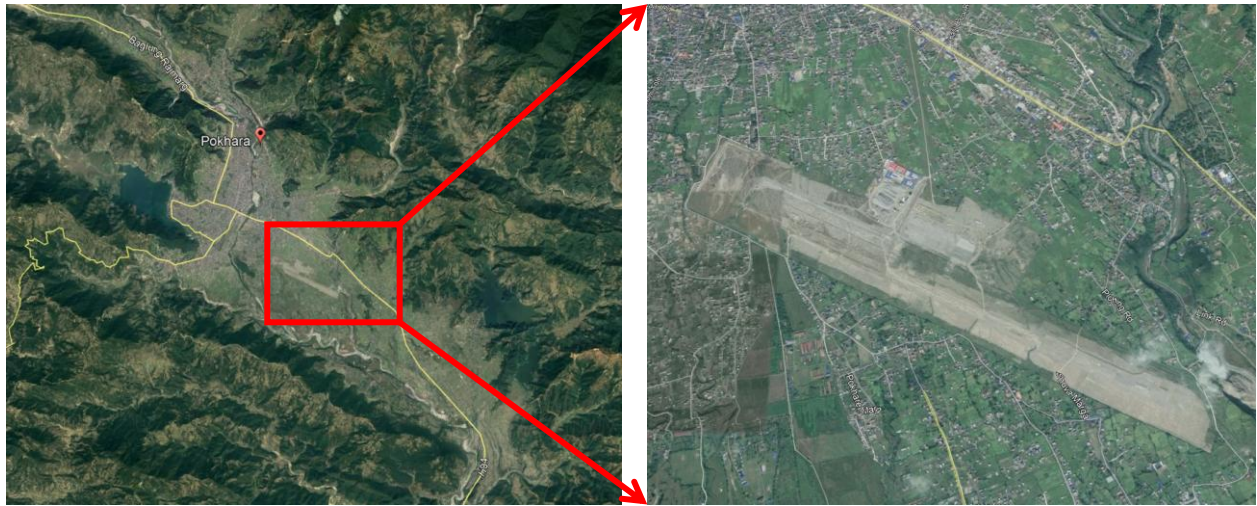


**Figure 2.** Study site covering the downtown area of Pokhara valley and its surrounding: right hand side picture shows the core firm land converted in to the builtup area.

### 3.2 Meteorological Data

Local meteorology especially, temperature, wind speed and direction play vital role for the generation, transport and dispersion of air pollution from the source to the surrounding location. Initial and boundary conditions in the modeling were set based on the available meteorology data. The meteorological data, such as wind speed, wind direction, rainfall data were retrieved from Department of Hydrology and Meteorology Pokhara. The data recorded at the station 866 which is located at  $28^{\circ}12'20.1''\text{N}$   $83^{\circ}58'24.8''\text{E}$  (6X4F+6CM) at the elevation of 827m has been referred in this study.

### 3.3 Air Flow and Air Dispersion Modelling

The structure and circulation pattern of the breeze varies in different geographic location, although many factors such as solar radiation, landuse pattern (i.e. surface albedo, roughness, soil moisture, anthropogenic heat, etc.), inversion height, potential temperature, external wind force, etc. affect its structure and pattern. The modeling domain for this study area is designed as in Fig. 3 where the sizes of outer, interim, and inner domains are  $42\text{ km} \times 32\text{ km}$ ,  $30\text{ km} \times 24\text{ km}$  and  $20\text{ km} \times 14\text{ km}$ , respectively. The resolutions of the outermost, interim and inner nested grids are 4 km, 2 km and 1 km, respectively.

The modeling period was selected in mid of April (Julian days 101 - 103) by considering dry and less rainy season when the potential temperature difference is sufficient for breeze generation. The Cloudless, non-rainy days were considered for increasing the accuracy of the input meteorological survey data. USGS30" resolution data (about 800m resolution at mid latitude) was used for extracting the geographic information and landuse data. The meteorology



data was used based on DHM 2018 data. The nudging and earth rotation options were set active. The rest of the parameters have been fixed as default values as summarized in the A2C manual.

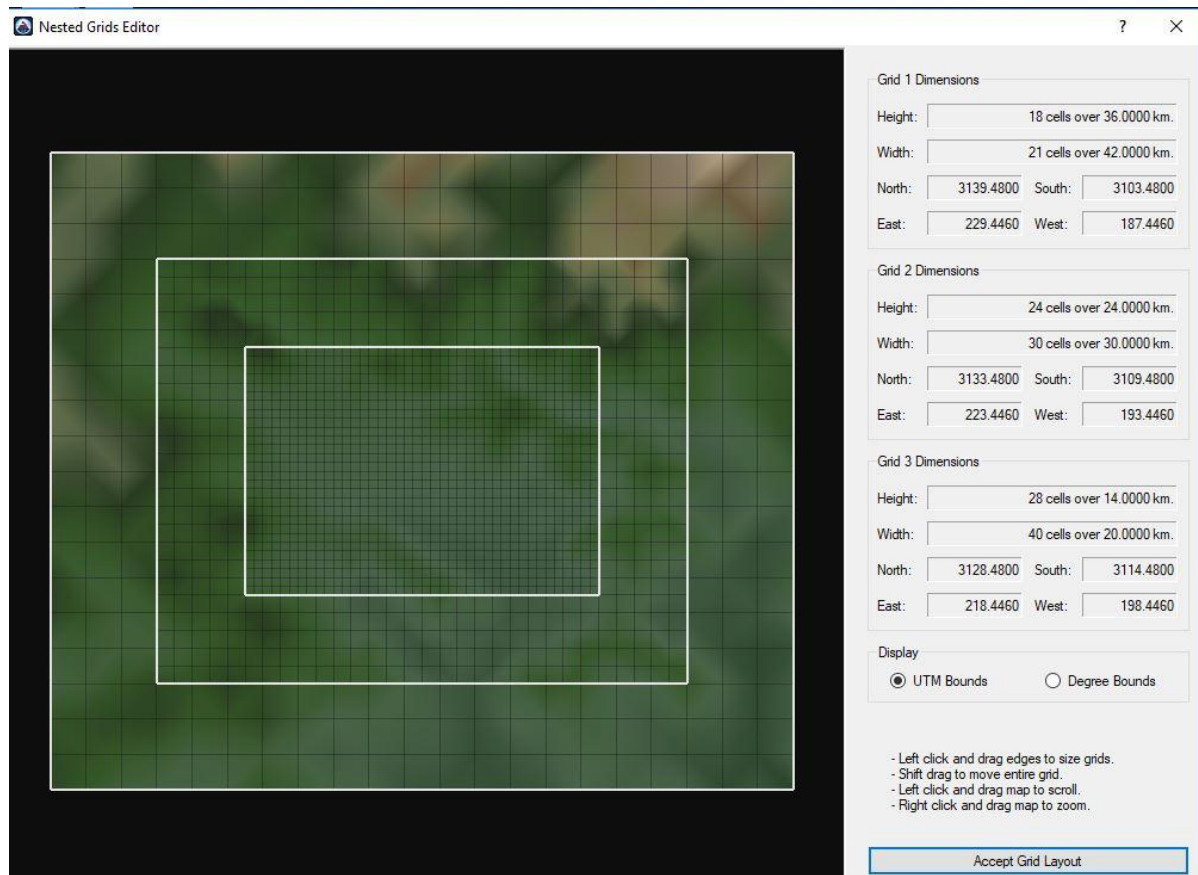


**Figure 3.** Modeling domain in different resolutions at outermost, interim and inner nested grids.

Two different techniques were applied for understanding the breeze structure and its influencing zone. In the first case, the breeze speed was sampled at different locations. In the second case, the point source Ps1 was set at the centre of the focused study site, where the puffs as emission continuously emitted from the area source with the diameter of 100 m and an altitude of 10 m. The puffs emitted from the point source were dispersed and transported by the breeze generated in the study domain. The structure of the pure breeze and its effective boundary length were estimated by analyzing wind speed, wind flow vectors and puffs dispersion patterns, respectively.

## 4. Results and Discussion

### 4.1 Meteorology of the Study Site

There are distinct four seasons in Pokhara where months from November to February are cold. Other months except midday of May – June are comfortable and warm. In general, winter months are dry and summer months are wet. More than 70% of annual rainfall has been observed during three months from June to August (Pokhrel and Ghimire, 2020). Majority of wind blows from north to south during the winter period and vice versa in the summer period. Figure 4 shows the wind speed and direction in different season of the year 2018. Most of the cases, wind blows from east and south-east direction with wind speed of 3 – 8 m/s in Pokhara. More than 10 m/s wind speed was frequently observed during the pre-monsoon period when

wind blows frequently from north-east and south-east direction. The high wind speed blows the fugitive dust from the surface and concentration of windblown dust can be observed in the pre-monsoon season than another season.

**Table 1.** Input parameters for the pure breeze modeling.

Parameters	Values	Remarks
Modeling domain	Nested grids = 3	$42 \times 36$ , $30 \times 24$ , $20 \times 14$ km <sup>2</sup>
Modeling period	Day = 101 - 103	Julian day
Wind speed (m/s)	0	No external wind
Wind direction	NA	
Ref. Pressure (mb)	1000	Ref. meteorological data
Potential temperature (°C)	23	Ref. meteorological data
Water temperature	25	
Height (m)	1000	As manual
Options	On	(nudging, earth rotation)

## 4.2 Air Flow Mechanism

A2C flow generates the meteorological information in the PBL based on the given initial and boundary condition data. Generally, the temperature of the earth surface varies with the variation of sun energy. The temperature differs significantly place to place due to the different landuse pattern and different specific heat capacities of landuse objects even though Sun energy is constant (Weil, 1988). In case of study area, most of the surface is covered by land and it is surrounded by green mountains followed by Himalayan in few kilometers far. After sunset, higher elevated mountain region releases heat faster than valley area, subsequently the mountain surface temperature becomes lower than the valley surface in late evening to early morning before sunrise. Consequently, the pressure above the valley surface becomes lower than pressure above the land surface which causes the dynamic air flow from mountain to the valley (mountain breeze) as in Fig. 5 (a, b and c). Mountain breeze gained its maximum speed just before sunrise around 6AM and then it reduces with the reduction on temperature difference between the surrounding mountain and the valley.

After sunrise, the high elevated land (mountain) surface heats faster than low elevated land (valley surface) as sun energy penetrates mountain surface before the valley surface. Correspondingly, the potential temperature difference between the mountain and the valley surface goes down, which results the collapse of the mountain breeze and reaches to transition stage around 9AM to 10AM. Figure 5 (d) shows the wind vectors just before the transition of mountain breeze to the valley breeze when very mild breeze can be observed. When the temperature of the mountain surface reaches considerably higher than the valley surface, the air above the mountain area rises up. Consequently, pressure above the mountain surface

becomes lower than the pressure above the valley surface where the air flows from higher pressure side to lower pressure, i.e. valley breeze as in Fig. 5 (e), (f). The mountain surface temperature diminishes faster than the valley surface temperature with the declination of sun radiation energy and hence the valley breeze continuously diminishes and reaches to the transition period again around 8PM to 10PM. The locally generated breeze and its boundary play vital role for the transport and diffusion of air pollution at that boundary. Moreover, the concentration of air pollution in certain locality vary with the varying the boundary layer (Fan et al.; Jeong, Lee and Lee, 2008; Jung, Pokhrel and Lee, 2009). A study shows that the katabatic winds had varied effects on pollution in different city regions, influenced by atmospheric conditions. Moreover, the meteorological factor such as temperature lapse rate, topography and surface coverage limit the air pollution dispersion (Shang et al., 2023).

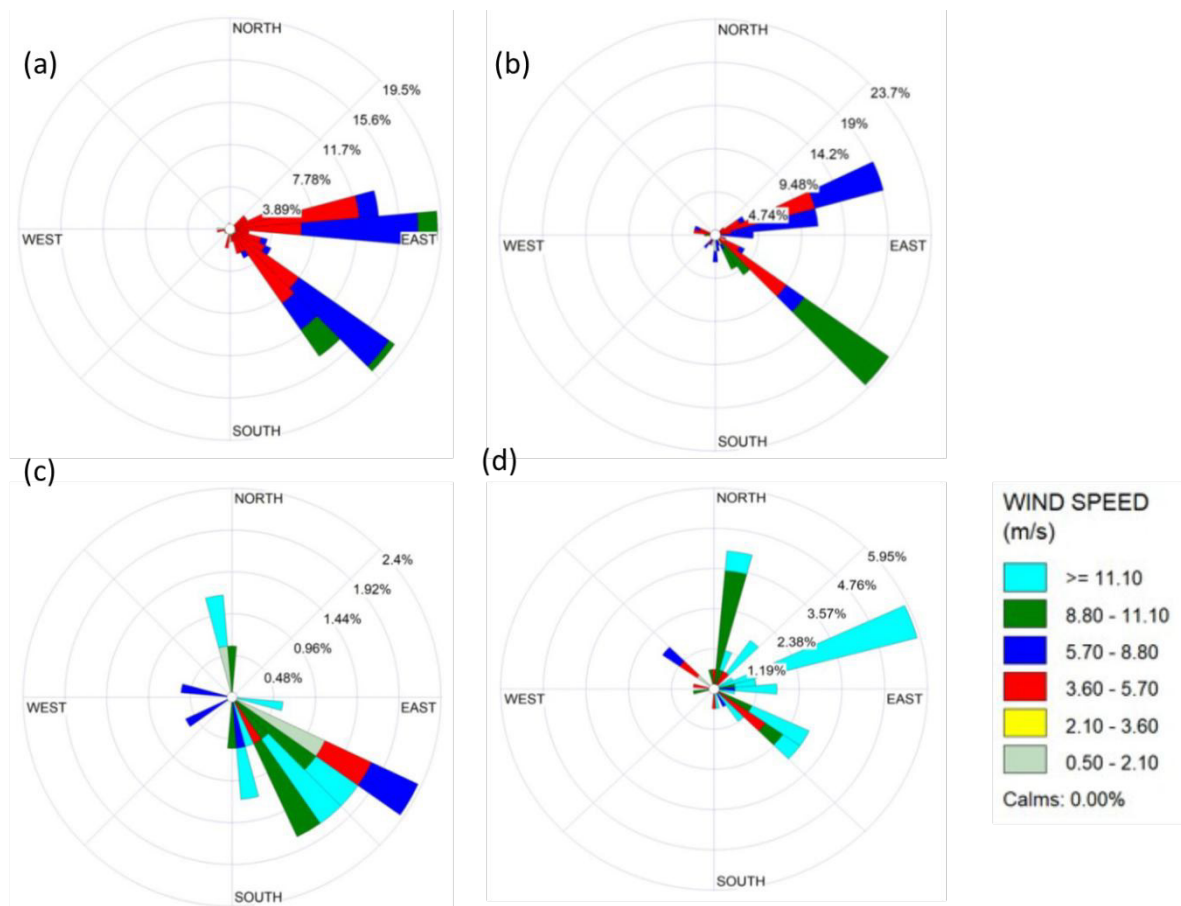
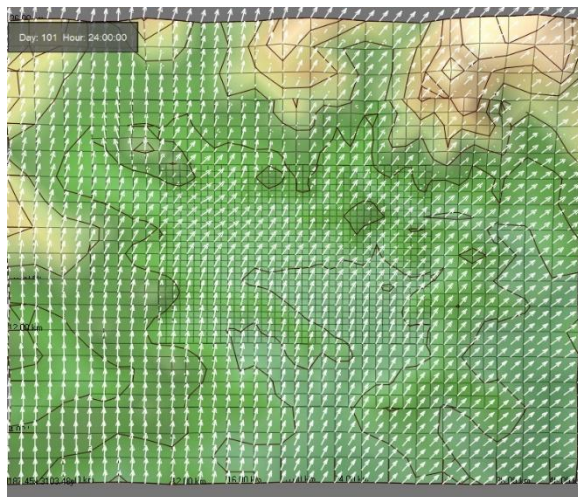
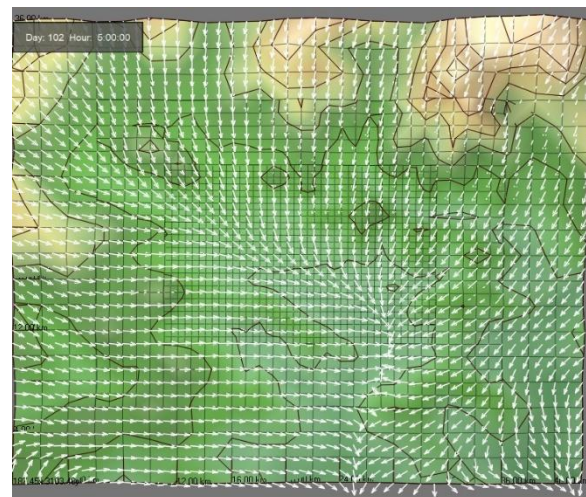


**Figure 4.** Windrose shows the wind profile during (a) Monsoon period, (b) Post-monsoon period, (c) Winter period and (d) Pre-monsoon period.

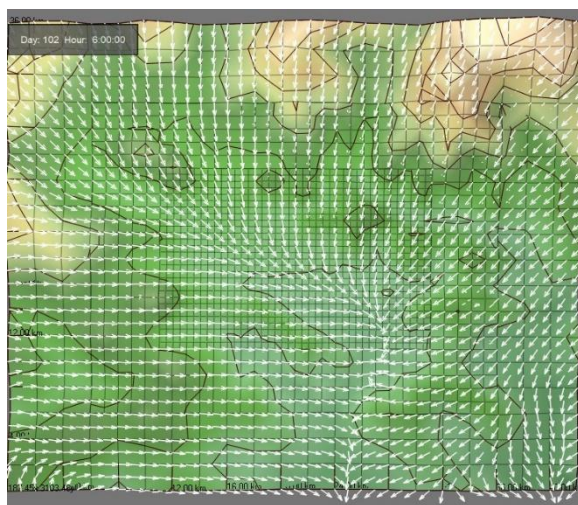




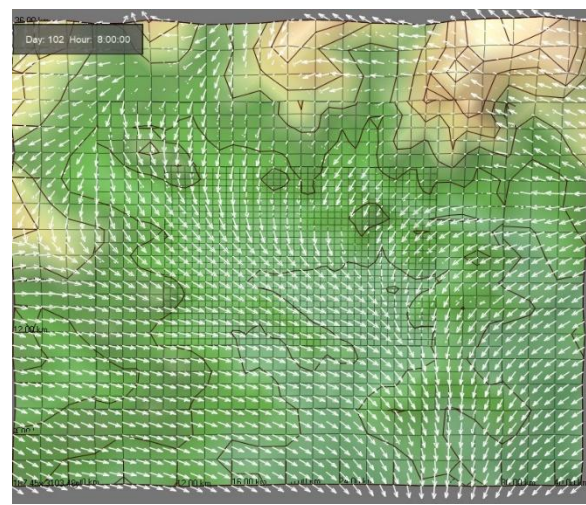
(a) Time 00:00



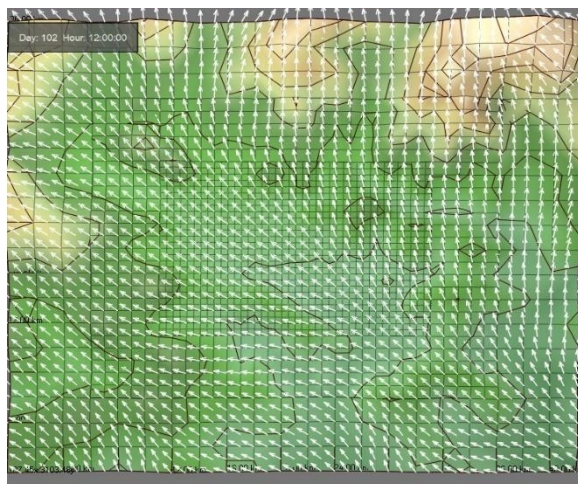
(b) Time 01:00



(c) Time 06:00



(d) Time 08:00



(e) Time 12:00



(f) Time 18:00

**Figure 5.** Diurnal changes of wind flow profile in the study area



### 4.3 Air Dispersion Mechanism

Transportation and dispersion of puffs from the sources depend on the local meteorological condition. Mountain breeze generates during late night to early morning when puffs transport and disperse to the valley side. Mountain breeze diminishes and changes to valley breeze after 10AM when the puffs near the source start to disperse towards mountain side and disperse above the mountain region as in Fig. (6).

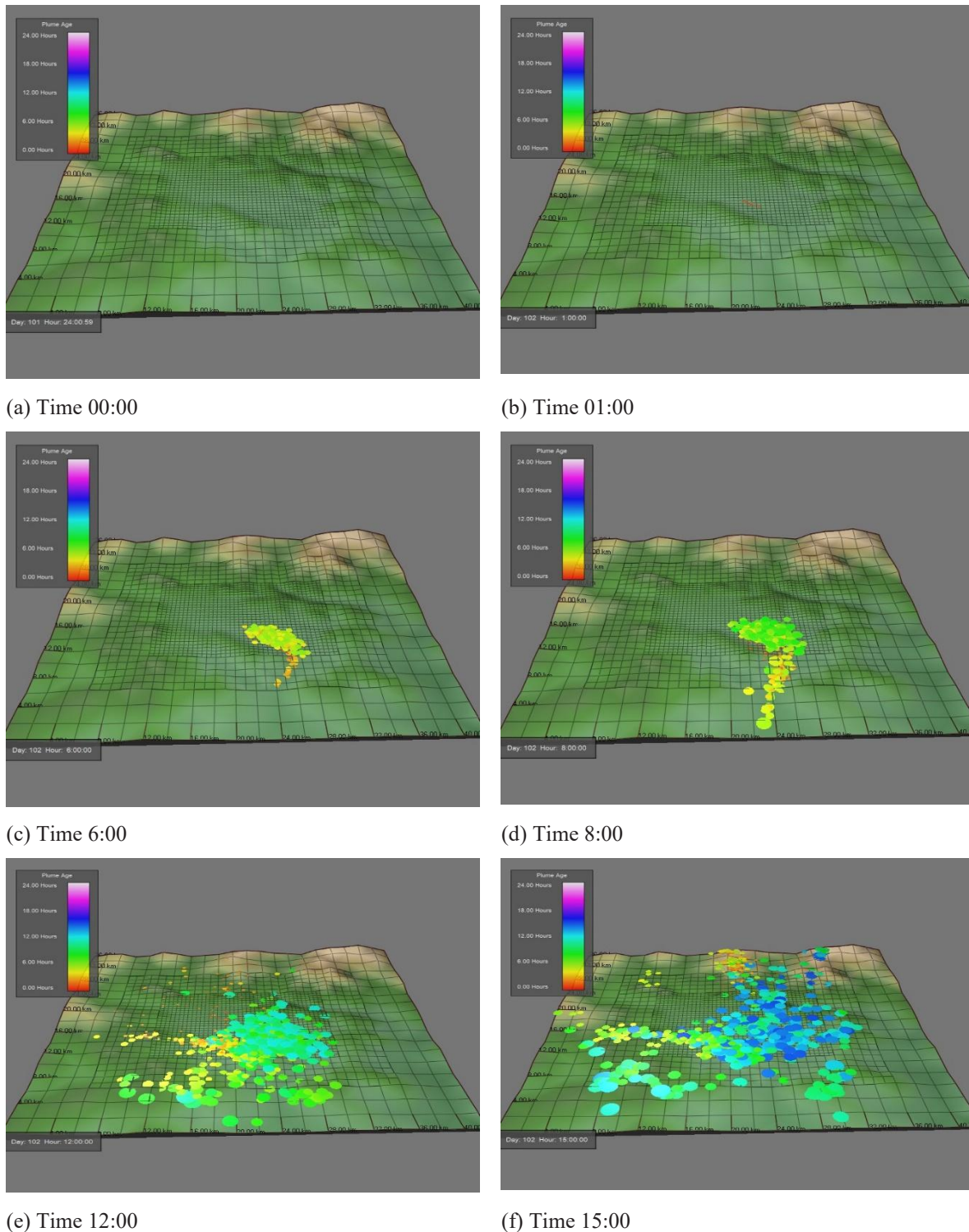


**Figure 6.** Puff dispersion from the source by locally generated breeze in the study domain.

Pokhara Regional International Airport (PRIA) has been in constructed and operation at the central area of Pokhara Valley. The puffs source in this study as in Fig. 6. (a) is located at the same location of PRIA site. The puffs in the modeling domain represent the pollutants generated from the construction site (PRIA). Figure 6 (b – f) shows the puff dispersion mechanism from source to the surrounding area at different time period. Puffs from the source transports towards south from late-night to the early-morning and it disperses around the high-altitude mountain region in the daytime. It shows that the pollutions generated from the construction site disperse in the mountain region by the locally generated wind. Similar study was conducted in the Sichuan Basin (SCB), China to identifying the impact of mountain valley breeze on ozone pollution. The mountain valley driven near-surface O<sub>3</sub> concentrations increased by 8.8%, with 12.7% and 50.0% deterioration in the O<sub>3</sub> light and moderate exceedance rates, respectively, on the western SCB edge (Zhang et al., 2024). Urban air pollutions generated from different sources such as construction site, industries, commercial sector, vehicular / aviation emission disperse inside the valley and its surrounding mountainous area. It may affect the air quality of the pristine mountain region. Therefore, policy should be developed for planned urbanization by considering urban air quality, bio-ecosystem and climate resilient society.

## 5. Conclusion

Pokhara has been recognized as one of the beautiful valleys because of its pristine nature and cool and clean environment. The valley has been changed rapidly in terms of its landuse as well as air quality. Local meteorology directly affected the urban comfort as well as air quality of the valley due to its driving effect on air pollution dispersion. Majority of breeze flows from north to south and vice-versa in Pokhara whereas the external wind dominates during the pre-monsoon period. A study was conducted to identify the air pollution dispersion mechanism in the valley using Lagrangian Approach. The simulation results for the study domain revealed that the air flows from the mountain region to the valley from the mid night to the early morning around 8 AM. As the mountain region get heated, the flow velocity decreases and reaches to the transition state around 09:00 AM – 10:00 AM. Then flow direction changes towards the Mountain region after 11 AM and wind speed is maximum around 2 PM to 3 PM. It is continuous till mid-night around 9 PM to 10 PM and again reaches to the transition period.

Urban air pollution generated in the valley area accumulated in the valley region in the mid-night to the early morning due to the effect of mountain breeze and it disperses around the upper air mostly above the mountain region. Mostly, the pollution generated nearby the mountain region disperses above the mountain region in the daytime. The pollution generated near the mountain region has significantly less impact to urban area where as the pollution generated from the urban area affects the air quality in the mountain region. Locally generated wind speed and its boundary plays the vital role for maintaining in the valley. It is concluded that the pollution generated from the different sources disperses around the valley and reached up to the mountain region which may degrade the quality of scenic vista.

## Acknowledgements

This research is partially supported by Pokhara University Research Center funded research grant number 01/074/75 (FRG AC). I would to thank all the supporting hands for completing this research.

## References

- Fan, S., Wang, B., Tesche, M., Engelmann, R., Althausen, A., Liu, J., Zhu, W., Fan, Q., Li, M., Ta, N., Song, L., Leong, K., 2008. Meteorological condition and structures of atmospheric boundary layer in October 2004 over Pearl River Delta area. *Atmospheric Environment*, 42, 6147-6186.
- Jacob, D. J., 1999. *Introduction to atmospheric chemistry*. Princeton University Press.
- Jeong, J., Lee, I.H., Lee, H., 2008. Estimation of the effective region of Sea/Land breeze in west coast using numerical modeling. *Journal of Korean Society for Atmospheric Environment*, 24, 2, 259-270.
- Jung, C.H., Pokhrel, R., Lee, H.K., 2009. The impact of power plants on the environment and region – Focus on Incheon area according to the 3rd electric support action plan. *Journal of Environmental Impact Assessment Korea*, 18, 4, 195-208.
- Laña, I., Ser, J. D., Padró, A., Vélez, M., Casanova-Mateo, C., 2016. The role of local urban traffic and meteorological conditions in air pollution: A data-based case study in Madrid, Spain. *Atmospheric Environment*, 145, Pages 424-438. <https://doi.org/10.1016/j.atmosenv.2016.09.052>.
- Pokhrel, R., Lee, H., 2011. Estimation of the effective zone of sea/land breeze in a coastal area. *Atmospheric Pollution Research*, 2, 106-115.
- Pokhrel, R., Ghimire, S. (2020) Numerical Simulation on Air Pollution Emission from the Construction Site and Its Dispersion in the Pokhara Valley. PURC, Pokhara University.
- Shang, J., Zhong, H-Y., Zhang, H-L., Li, B., Wang, X-X., Zhao, F-Y., Li, Y., 2023. Diode effects on street canyon ventilation in valley city: Temperature inversion and calm geostrophic wind. *Building and Environment*. 244, 10839.
- Wond, N H., Chen, Y., 2009. *Tropical Urban Heat Island: Climate, Buildings and Greenery*. Taylor and Francis.
- Weil, J. C., 1988a. Dispersion in the convective boundary layer: Lectures on Air Pollution Modeling. Venkatram, A. and Wyngaard, J. C. *American Meteorological Society*, 167-227.
- Yamada, T., 1981. A numerical simulation of nocturnal drainage flow. *Journal of The Meteorological Society of Japan*, 59, 108-122.
- Yamada, T., Kao, J.C.Y., Bunker, S., 1989. Airflow and air quality simulations over the western mountainous region with a four-dimensional data assimilation technique. *Atmospheric Environment* 23, 539-554.
- Yamada, T., 1999. A numerical simulation of urbanization on the local climate. *Journal of Wind Engineering and Industrial Aerodynamics*, 81, 1-19.
- Yamada, T., 2004. Merging CFD and atmospheric modeling capabilities to simulate airflows and dispersion in urban areas. *Journal of Computational Fluid Dynamics (CFD J.)* 13(2):47, 329-341.
- Zhang, Y., Zhao, T., Sun, X., Bai, Y., Shu, Z., Fu, W., Lu, Z., Wang, X., 2024. Ozone pollution aggravated by mountain-valley breeze over the western Sichuan Basin, Southwest China. *Chemosphere*, 361, 142445. <https://doi.org/10.1016/j.chemosphere.2024.142445>

## Assessment of Structural Rebar Wastage of Reinforced Cement Concrete Buildings: A Case Study of School Building Type Designs in Kathmandu

Sanjaya Dahal<sup>1\*</sup>, Govind Prasad Lamichhane<sup>1</sup>, Safal Subedi<sup>2</sup>

<sup>1</sup> Pokhara Engineering College, Pokhara University

<sup>2</sup> Thapathali Campus, Institute of Engineering, Tribhuvan University

\*Corresponding email: [er.sanjayadahal@gmail.com](mailto:er.sanjayadahal@gmail.com)



Pokhara Engineering College Journal (ISSN: 3021-9795), Copyright © [2025] The Author(s). Published by Pokhara Engineering College, distributed under the terms of the Creative Commons Attribution 4.0 International License (CC BY-NC 4.0).

Received: 28-November-2024; Revised: 28-January-2025; Accepted: 31-January-2025

### Abstract

Economic growth and urbanization in developing countries have led to significant construction activities, resulting in large amounts of waste, which is recognized as a key problem in various cities. In this regard, the management of waste is recommended as an important and integrated task in project execution. In this study, rebar waste generated from construction activities of educational building projects in Kathmandu is examined. A qualitative approach was followed, using four types of school building designs as case studies. Site observations, data collection, and analysis of the selected buildings were carried out. The minimum and maximum cutting waste of structural rebar were found to be 11.52% and 15.21%, respectively. The results of each project are presented, and a cross-case analysis was conducted to compare similarities and differences in factors related to waste generation.

**Keywords:** *Cutting Waste, Rebar Offcuts, School Building, Sustainable Construction*

### 1 Introduction

The construction of reinforced concrete (RC) structures is accompanied by substantial consumption of concrete and rebar. It has been reported that global concrete consumption reached approximately 10 billion m<sup>3</sup> in 2012, with demand for RC structures increasing due to global economic development (Khondoker, 2021). Rebar, a key component of RC structures, is identified as a significant contributor to CO<sub>2</sub> emissions, with an embodied CO<sub>2</sub> (ECO<sub>2</sub>) of 872 kg-ECO<sub>2</sub>/t, which is approximately 9.2 times higher than that of concrete (Porwal & Hewage, 2012). The urgent need to minimize rebar-cutting waste is highlighted, as it directly influences greenhouse gas emissions and sustainability (Lee, et al., 2020). Research has indicated that cutting waste from rebar ranges between 3% and 8%, depending on construction practices and country-specific factors (Lee, et al., 2020).

The global rise in rebar off-cuts has been associated with unnecessary costs and increased CO<sub>2</sub> emissions during manufacturing, transportation, and processing (Kwon, et al., 2021). Near-zero cutting waste has been identified as a goal for researchers since the introduction of the Cutting Stock Problem (CSP) in 1939 (Nadoushani, et al., 2016). However, near-zero waste has not yet been achieved, particularly in Nepal, where sustainable construction practices and energy-efficient strategies are often neglected. The assessment of rebar waste is considered



critical for understanding its environmental impact and supporting the formulation of policies aimed at promoting sustainable construction.

Rebar, typically supplied in standard lengths (e.g., 12m in Nepal), is often inefficiently utilized due to inconsistent cutting practices. Cutting decisions are typically made based on workers' judgment, leading to significant material wastage. In developing countries, construction and demolition waste is estimated to account for approximately 40% of total solid waste (Rode, et al., 2013), with 5%-8% originating from residential construction (Poon, et al., 2004). This waste is characterized by minimal salvage value, and improper handling has been associated with increased risks to workers. Minimizing such waste is considered essential for sustainable construction, as it reduces environmental impacts and enhances resource efficiency. The assessment of cutting waste is identified as a critical first step in achieving these goals (Danatzko & Sezen, M.ASCE, 2011).

Rebar cutting waste is modeled and quantified in this study to assess the embodied energy of rebar, and measures are proposed to minimize carbon emissions from construction activities.

## **2 Materials and Methods**

### **2.1 Research Site:**

Nepal is recognized as one of the most hazard-prone countries in the world, with earthquakes, landslides, and floods identified as the most severe hazards. The frequency and intensity of weather-related hazards, including landslides, floods, and droughts, are expected to increase due to climate change. Seismic events are known to trigger secondary hazards such as landslides, floods, and fires. Although massive earthquakes occur occasionally, they result in significant casualties, physical damage, and economic losses. The damages and losses caused by the devastating 2015 Gorkha earthquake were assessed at \$7 billion, with 8,790 casualties, 22,300 injuries, 7,800 schools damaged, and approximately eight million people affected, accounting for nearly 29% of the population (National planning commission, Government of Nepal, 2015). It has been estimated that over 72% of the school buildings in the country's 35,000 schools were unsafe and required seismic retrofitting. The 2016 Structural Integrity Damage Assessment (SIDA) reported that 2,234 schools were heavily damaged and rendered unusable in fourteen districts severely affected by the 2015 earthquake (National planning commission, Government of Nepal, 2015). For the reconstruction of schools, several design types were developed. Among these designs, 3-C-12, 3-C-9, 3-C-7, and 4-C-16 from the Kathmandu district were selected for this study. The general and structural parameters are presented below in Table 1 and Table 2 respectively.

### **2.2 Research Methodology:**

The research was conducted using a pragmatic paradigm to assess the cutting waste of structural reinforcement steel bars during the construction of RCC buildings for the implementation of sustainable construction. Both qualitative and quantitative methods were employed, as they were deemed relevant for addressing research objectives. Data collection, analysis, and interpretation methods were applied.

The study was carried out based on an explanatory approach, incorporating a literature review and case study. Explanatory research, which focuses on understanding relationships between variables and their implications in the past and future, was employed to incorporate a quantitative approach. The variation trends of structural rebar cutting procedures and the environmental impacts of rebar waste were analyzed and compared. Subsequently, a case study site and building were selected to gather data on building materials, size, and other parameters required for rebar cutting waste analysis.

In this research, the cutting waste of rebar in RC school buildings was reviewed using the positivist paradigm. The bar bending schedule was analyzed using MS Excel and AutoCAD. The data obtained were further processed using the solver tool in MS Excel. These data were analyzed and compared. Cutting waste from a building's structural rebar was treated as quantitative data. The processed data was used to calculate the embodied energy to assess the environmental impact of structural rebar wastage. Based on the findings, an interpretive approach to building research was adopted to propose measures for minimizing reinforcement cutting waste. Measures for rebar optimization were proposed based on the findings from the analysis and literature review.

**Table 1:** General parameters of school building (Type designs).

Block ID	3-C-12	3-C-9	3-C-7	4-C-16
Structural Topology	RCC Frame Structure	RCC Frame Structure	RCC Frame Structure	RCC Frame Structure
No. of Story	G+2 (3 Storey)	G+2 (3 Storey)	G+2 (3 Storey)	G+3 (4 Storey)
Length of the Building	31 m	23 m	18 m	31 m
Breadth of the Building	9 m	9 m	8.5 m	9 m
Height of the Building	13.55 m	13.5 m	13.55 m	16.55 m
Wall Type	Brick Masonry in Cement Mortar	Brick Masonry in Cement Mortar	Brick Masonry in Cement Mortar	Brick Masonry in Cement Mortar
Floor Type	RCC Slab	RCC Slab	RCC Slab	RCC Slab
Door and Windows	Metal (Frame and Panel)	Metal (Frame and Panel)	Metal (Frame and Panel)	Metal (Frame and Panel)

**Table 2:** Structural parameters of school building (Type designs).

Concrete Grade	M20	M20	M20	M20
Column	500x500	500x500	500x500	500x500
Foundation Beam	230x355 mm	230x355 mm	230x355 mm	230x355 mm
Plinth Beam	230x355 mm	230x355 mm	230x355 mm	230x355 mm
Main Beam	350x550 mm	350x550 mm	350x550 mm	350x550 mm
Secondary Beam	230x400 mm	230x400 mm	230x400 mm	230x400 mm
Slab	125 mm	125 mm	125 mm	125 mm
Waist Slab	200 mm	200 mm	200 mm	200 mm
Footing	F1=2.7 x2.7m, F2=3.6 x 3.6m, CF1=5.8x3.2m, CF2=6.3x 3.8m	F1=2.7x2.7m, F2=3.5x 3.5m, CF1=5.67x3.0m ,CF2=6.4x3.8m	F1=2.9m x2.9m, F2= 3.7m x 3.7m, CF1=6.3mx3.6m , CF2=6.3mx 4.5m	F1=2.7x2.7m, F2=3.6x3.6m, CF1=5.8x3.2m ,CF2=6.3x 3.8m
Foundation Depth	1.2. m, 1.65 m (From ground level)	1.2. m, 1.65 m (From ground level)	1.2. m, 1.65 m (From ground level)	1.2. m, 1.65 m (From ground level)
Floor height	3.0 m	3.0 m	3.0 m	3.0 m
Soil Type	SBC 100kN/m <sup>2</sup> , Type III as per IS1893:2002	SBC 100kN/m <sup>2</sup> , Type III as per IS1893:2002	SBC 100kN/m <sup>2</sup> , Type III as per IS1893:2002	SBC 100kN/m <sup>2</sup> , Type III as per IS1893:2002
Wall Type	230 mm Brick Masonry	230 mm Brick Masonry	230 mm Brick Masonry	230 mm Brick Masonry
Floor Type	RCC Slab on all floors	RCC Slab on all floors	RCC Slab on all floors	RCC Slab on all floors

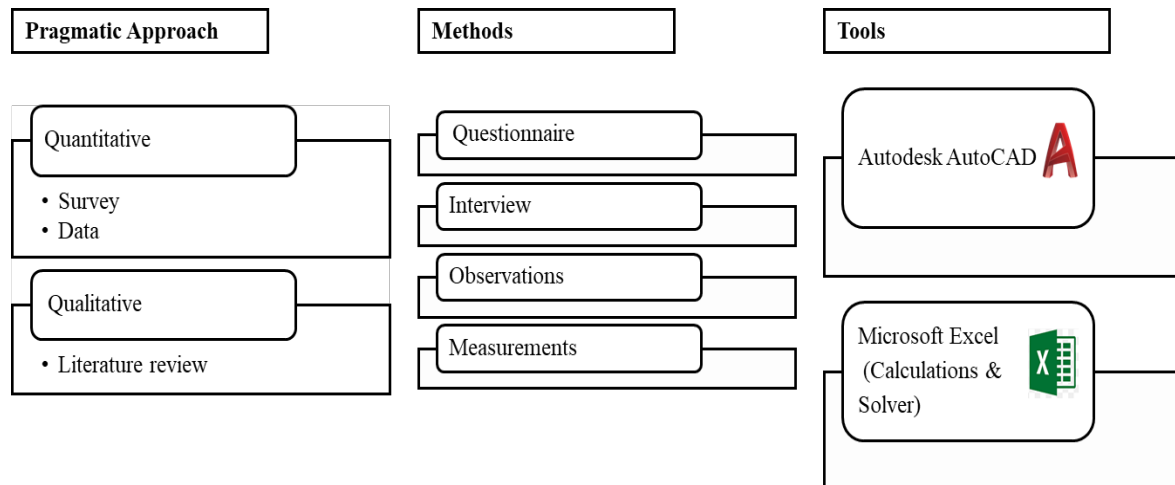


Figure 1: Research methodology

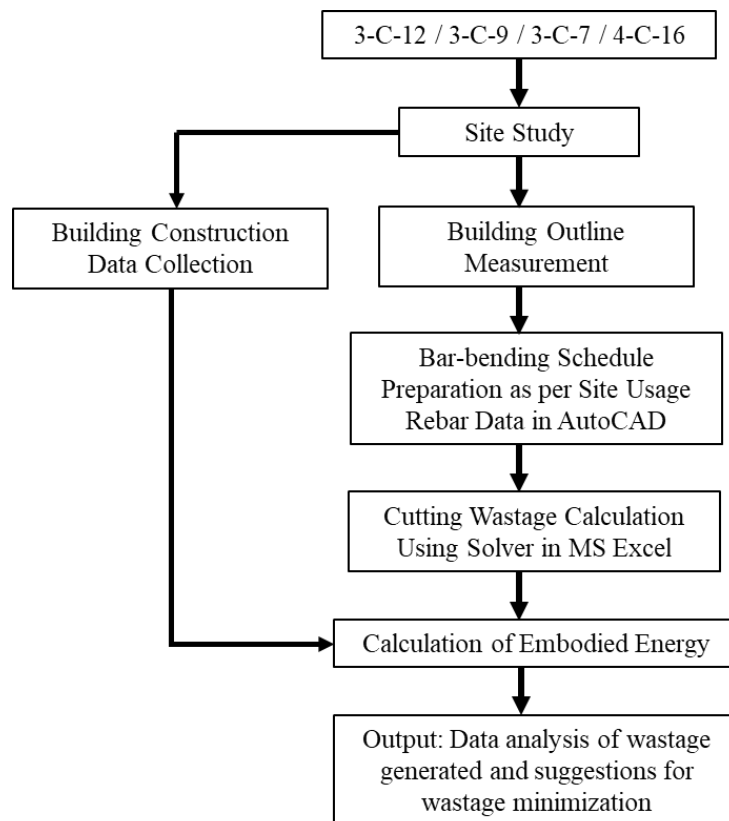


Figure 2: Working framework of study

### 2.3 Methods for Analysis:

For the assessment of cutting waste in structural reinforcement bars, the bar bending schedule for each type of design was prepared using data obtained from site measurements and drawings. The data were then analyzed using the solver tool in MS Excel.

An algorithm was proposed for solver to generate variants of cutting rods that resulted in the least waste. The algorithm involved analyzing all possible sets of bars of required lengths whose total length did not exceed the standard rod length. For each required bar length, the



maximum number of bars that could be obtained from a standard-length rod was calculated. For example, from a rod with a length of 12 m, a maximum of 12 bars of 1.0 m, 8 bars of 1.5 m, and 6 bars of 2.0 m could be obtained. The total number of combinations of these three bar types was calculated as 576, which is the product of the three numbers: 12, 8, and 6. In general, this number (K) was calculated using the formula provided by Matviyishyn and Janiak (Matviyishyn & Janiak, 2019).

$$K = \prod_{j=1}^n \frac{L}{d_j} \quad (1)$$

Where,

L is the standard length of rods used for bar cutting (in the example presented L=12 m);

d<sub>j</sub> is the length of bar of j type.

n is the number of types.

All possible options for cutting rods into bars of the required lengths were generated using this algorithm. The algorithm was implemented in a Microsoft Excel spreadsheet through a developed VBA macro. The generated options varied in terms of the length of waste remaining after cutting the steel rod. The selection of combinations from these options was made based on the data regarding the required number of bars of specific lengths.

### 3 Results and Discussion

#### 3.1 Scenario 1: 3-C-12

The total cutting waste obtained using solver is 7069 kg, which is 11.52% of the total stock rebar. Result thus obtained after calculations are presented below.

**Table 3:** Total cutting waste using solver in 3-C-12.

Rebar diameter	8mm	10mm	12mm	16mm	20mm	Total quantity(kg)
Stock weight(kg)	15779	14490	4486	19005	14654	68414
Finish weight(kg)	14536	13782	3941	17228	11859	61346
Scrap/offcut(kg)	1244	708	545	1777	2795	7069
Usage %	23.70%	22.47%	6.42%	28.08%	19.33%	100%
Scrap/offcut %	8.56%	5.14%	13.83%	10.31%	23.57%	11.52%

From the Table 3, it is observed that the highest quantity of rebar used is 16 mm in diameter, accounting for 28.08% of the total, as it is incorporated into almost all structural components, including footings, columns, beams, and staircases. In contrast, the lowest quantity of rebar used is 12 mm in diameter, comprising 6.42%, and is primarily utilized in footings and beams. However, the highest offcut wastage is recorded in 20 mm diameter rebar (23.57%), which is employed in columns and beams. The most significant wastage occurs in columns due to restrictions on the lapping zone, which is permitted to extend only up to half the height of the column. Furthermore, no more than 50% of the rebar can be spliced at a single position (IS 13920:1993, n.d.), thereby limiting the optimization of rebar cut-offs.

Figure 3 illustrates the distribution of rebar usage and cutting waste by structural component. According to the figure, beams account for the highest rebar consumption, followed by columns and slabs. However, columns contribute the most to cutting waste, followed by beams and slabs.

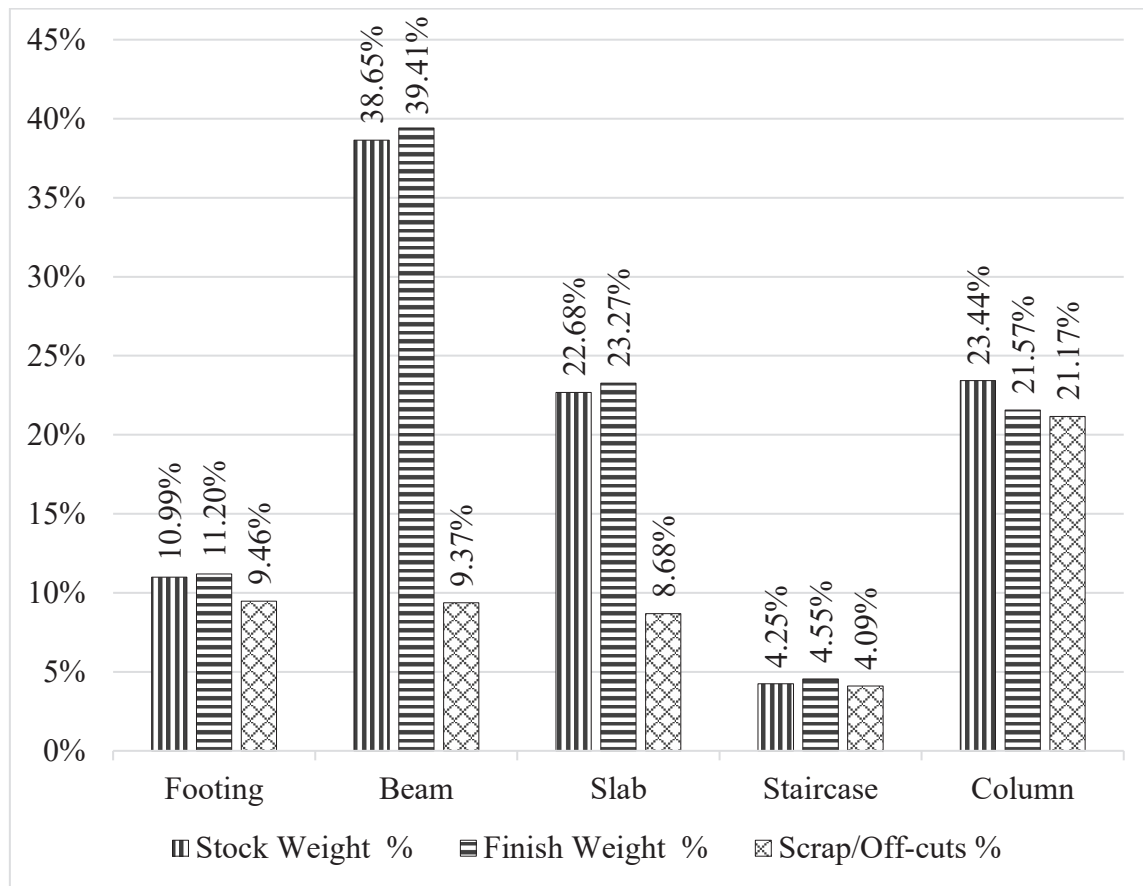


Figure 3: Cutting waste by structural component in 3-C-12.

### 3.1.1 Embodied energy of rebar

The embodied energy associated with the quantity of rebar obtained from bar bending schedule is shown below in the Table 4.

Table 4 : Embodied energy calculation of rebar in 3-C-12.

Embodied energy coefficient = 32.24 MJ/kg (Praseeda, et al., 2014)		
	Weight of Rebar (kg)	Embodied Energy (GJ)
Stock Weight (kg)	68414	2205.67
Finish Weight (kg)	61346	1977.79
Scrap/Off-cuts weight (kg)	7069	227.90

### 3.1.2 Cost rates for embodied carbon dioxide

Total embodied energy of off-cuts = 227.90 GJ

$$= 227.90 \times 0.24 \text{ ton}$$

$$= 54.69 \text{ ton}$$

Environmental cost of the emission of one ton of CO<sub>2</sub> in 2022 =194.28 euros

$$\begin{aligned}\text{Total environment cost of the emission of CO}_2 &= 54.69 \times 194.28 \\ &= 10626.55 \text{ euros}\end{aligned}$$

### 3.2 Scenario 2 : 3-C-9

The total cutting waste obtained using solver is 6711 kg, which is 13.43% of the total stock rebar. Result thus obtained after calculations are presented below.

**Table 5:** Total cutting waste using solver in 3-C-9.

Rebar diameter	8mm	10mm	12mm	16mm	20mm	Total quantity(kg)
Stock weight(kg)	7740	11809	4124	16636	16371	56681
Finish weight(kg)	7379	11234	3534	15034	12790	49970
Scrap/offcut(kg)	362	576	590	1602	3581	6711
Usage %	14.77%	22.48%	7.07%	30.09%	25.59%	100%
Scrap/offcut %	4.90%	5.13%	16.68%	10.66%	28.00%	13.43%

From the Table 5 , it is observed that the highest quantity of rebar used is 16 mm in diameter, accounting for 30.09% of the total, as it is incorporated into almost all structural components, including footings, columns, beams, and staircases. In contrast, the lowest quantity of rebar used is 12 mm in diameter, comprising 7.07%, and is primarily utilized in footings and beams. However, the highest offcut wastage is recorded in 20 mm diameter rebar (28.00%), which is employed in columns and beams. The most significant wastage occurs in columns due to restrictions on the lapping zone, which is permitted to extend only up to half the height of the column. Furthermore, no more than 50% of the rebar can be spliced at a single position (IS 13920:1993, n.d.), thereby limiting the optimization of rebar cut-offs.

Figure 4 illustrates the distribution of rebar usage and cutting waste by structural component. According to the figure, beams account for the highest rebar consumption, followed by columns and slabs. However, columns contribute the most to cutting waste, followed by beams and slabs.

#### 3.2.1 Embodied energy of rebar

The embodied energy associated with the quantity of rebar obtained from the bar bending schedule is shown below in Table 6.

**Table 6:** Embodied energy calculation of rebar in 3-C-9.

Embodied energy coefficient = 32.24 MJ/kg (Praseeda, et al., 2014)		
	Weight of Rebar (kg)	Embodied Energy (GJ)
Stock Weight (kg)	56681	1827.39
Finish Weight (kg)	49970	1611.03
Scrap/Off-cuts weight (kg)	6711	216.36

### 3.2.2 Cost rates for embodied carbon dioxide

Total embodied energy of off-cuts = 216.36 GJ

$$= 216.36 \times 0.24 \text{ ton}$$

$$= 51.92 \text{ ton}$$

Environmental cost of the emission of one ton of CO<sub>2</sub> in 2022 = 194.28 euros

Total environment cost of the emission of CO<sub>2</sub> = 51.92 x 194.28

$$= 10088.38 \text{ euros}$$

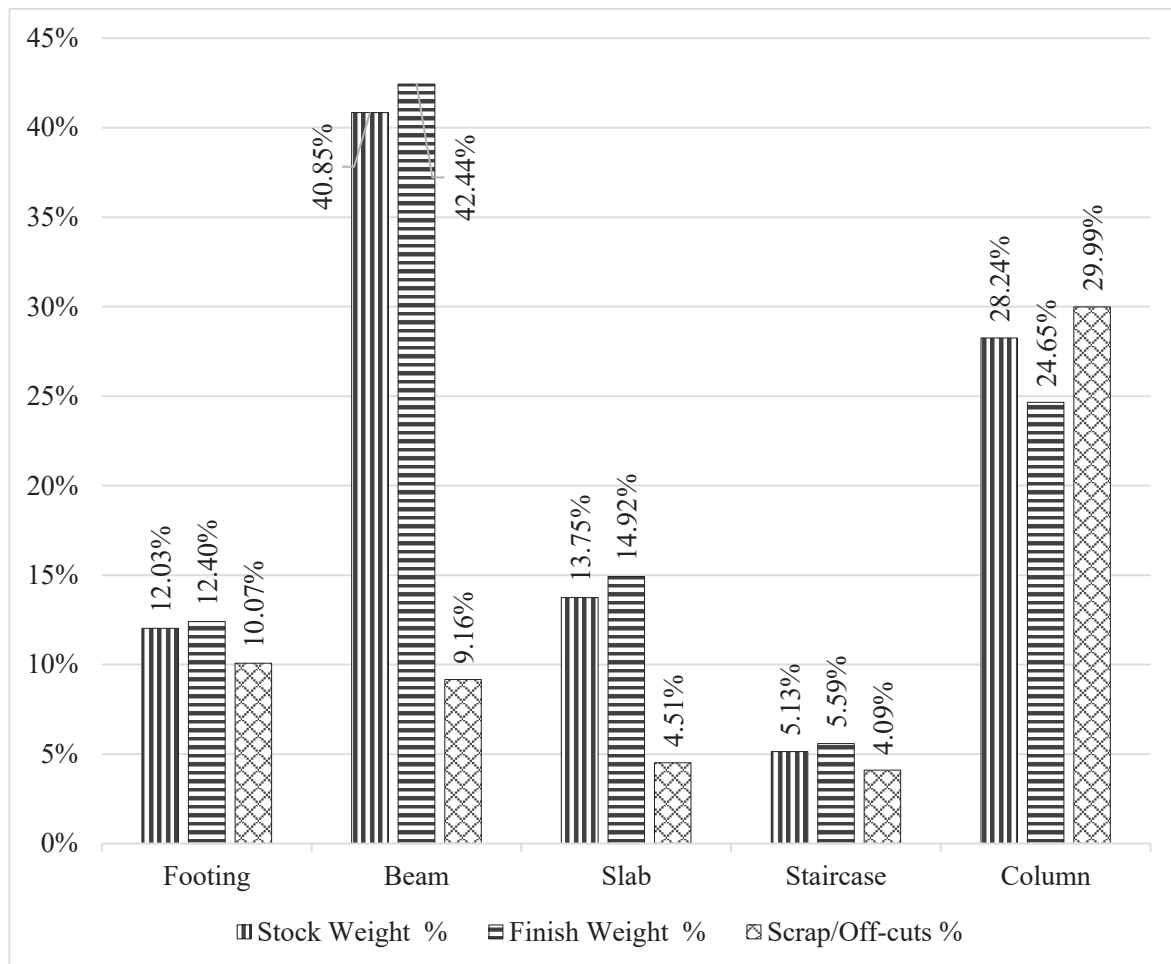


Figure 4: Cutting waste by structural components in 3-C-9

### 3.3 Scenario 3 : 3-C-7

The total cutting waste obtained using solver is 5090 kg, which is 12.49% of the total stock rebar. Result thus obtained after calculations are presented below.

From the Table 7, it is evident that 16 mm diameter rebar constitutes the highest proportion (35.46%) of the total rebar used, as it is incorporated into nearly all structural components, including footings, columns, beams, and staircases. In contrast, 25 mm diameter rebar accounts for the lowest percentage (0.27%) and is entirely utilized in columns. However, the greatest offcut wastage is observed in 25 mm diameter rebar (65.52%), followed by 16 mm diameter

rebar. This can be attributed to the increased lap length required for larger-diameter rebars and the use of 25 mm rebar in ground-floor columns, extending up to mid-height of the first floor. The positioning of lap splices for different rebar sizes results in significant offcuts for 25 mm rebar, as splicing restrictions prevent their full utilization, leading to greater material waste. Based on this analysis, it can be inferred that columns contribute the most to rebar wastage due to limitations in the lapping zone, where splicing is restricted to half the column height and no more than 50% of the rebar can be spliced at a single location (IS 13920:1993, n.d.).

Figure 5 presents the distribution of rebar usage and cutting waste across structural components. As depicted in the figure, beams account for the highest rebar consumption, followed by columns and footings. However, columns generate the most cutting waste, with beams and footings contributing comparatively less.

**Table 7:** Total cutting waste using solver in 3-C-7.

Rebar diameter	8mm	10mm	12mm	16mm	20mm	25mm	Total quantity(kg)
Stock weight(kg)	5792	10329	3783	16750	9000	185	45838
Finish weight(kg)	5368	9799	3341	14449	7679	112	40748
Scrap/offcut(kg)	424	529	442	2301	1321	73	5090

Usage %	13.17%	24.05%	8.20%	35.46%	18.84%	0.27%	100%
Scrap/offcut %	7.90%	5.40%	13.23%	15.92%	17.20%	65.52%	12.49%

Component	Stock Weight %	Finish Weight %	Loss %
Footing	15.57%	15.20%	10.07%
Beam	34.46%	38.47%	9.36%
Slab	14.11%	14.19%	6.79%
Staircase	6.64%	6.86%	4.09%
Column	29.22%	25.28%	24.18%

**Figure 5:** Cutting waste by structural components in 3-C-7.

### 3.3.1 Embodied energy of rebar

The embodied energy associated with the quantity of rebar obtained from bar bending schedule is shown below in the Table 8.

**Table 8:** Embodied energy calculation of rebar in 3-C-7.

Embodied energy coefficient = 32.24 MJ/kg (Praseeda, et al., 2014)		
	Weight of Rebar (kg)	Embodied Energy (GJ)
Stock Weight (kg)	43780	1411.45
Finish Weight (kg)	40748	1313.71
Scrap/Off-cuts weight (kg)	5090	164.10

### 3.3.2 Cost rates for embodied carbon dioxide

Total embodied energy of off-cuts = 164.10 GJ

$$= 164.10 \times 0.24 \text{ ton}$$

$$= 39.38 \text{ ton}$$

Environmental cost of the emission of one ton of CO<sub>2</sub> in 2022 = 194.28 euros

Total environment cost of the emission of CO<sub>2</sub> = 39.38 x 194.28

$$= 7651.59 \text{ euros}$$

### 3.4 Scenario 4 : 4-C-16

The total cutting waste obtained using solver is 12323 kg, which is 15.21% of the total stock rebar. Result thus obtained after calculations are presented below.

**Table 9:** Total cutting waste using solver in 4-C-16.

Rebar diameter	8mm	10mm	12mm	16mm	20mm	25mm	Total quantity(kg)
Stock weight(kg)	20382	18814	4891	20236	22381	6661	93365
Finish weight(kg)	18770	17900	4277	18452	17263	4381	81043
Scrap/offcut(kg)	1612	914	614	1785	5118	2281	12323
Usage %	23.16%	22.09%	5.28%	22.77%	21.30%	5.41%	100%
Scrap/offcut %	8.59%	5.11%	14.35%	9.67%	29.65%	52.07%	15.21%

Table 9 indicates that the 8 mm diameter rebar constitutes the highest proportion (23.16%) of the total rebar used, followed by 16 mm (22.77%) and 10 mm (22.09%) diameter rebars. In contrast, 12 mm (5.28%) and 25 mm (5.41%) diameter rebars account for the lowest

proportions. However, the highest cutting wastage is observed in 25 mm diameter rebar (52.07%), followed by 20 mm diameter rebar (29.65%). This can be attributed to the greater lap length required for larger-diameter rebars, as 25 mm rebar is primarily used in ground-floor and first-floor columns, extending up to the mid-height of the subsequent floor. The positioning of lap splices for 25 mm and 20 mm rebars results in higher offcuts, as splicing restrictions prevent complete utilization of these lengths, leading to increased material waste. Based on this analysis, it can be inferred that columns contribute the most to rebar waste, as the lapping zone is restricted to half the column height, and no more than 50% of the rebar can be spliced at a single location (IS 13920:1993, n.d.).

Figure 6 presents the distribution of rebar usage and cutting waste across structural components. According to the figure, beams account for the highest rebar consumption, followed by columns and slabs. However, columns generate the most cutting waste, followed by beams and footings.

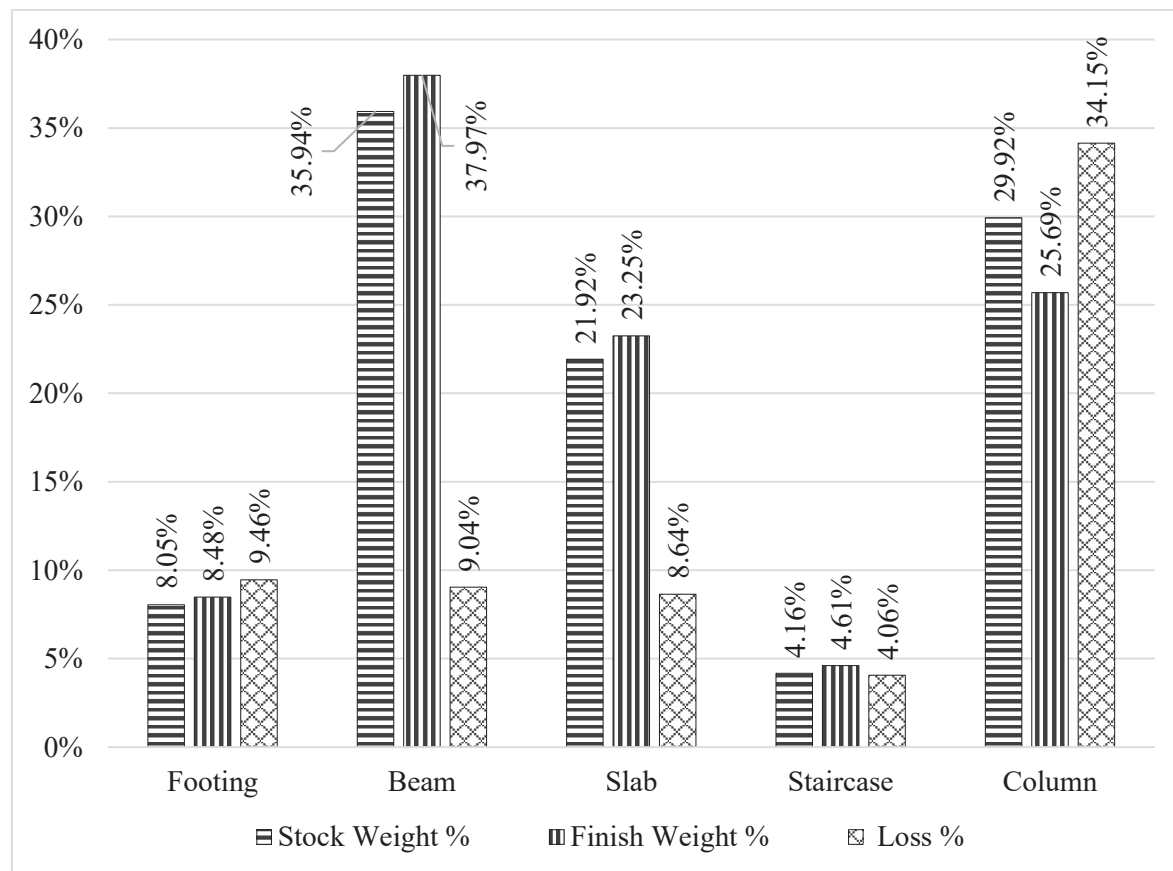


Figure 6: Cutting waste by structural component in 4-C-16

### 3.4.1 Embodied energy of rebar

The embodied energy associated with the quantity of rebar obtained from bar bending schedule is shown below in the Table 10.

Table 10: Embodied energy calculation of rebar in 4-C-16.

Embodied energy coefficient = 32.24 MJ/kg (Praseeda, et al., 2014)	
Weight of Rebar (kg)	Embodied Energy (GJ)

Stock Weight (kg)	93365	3010.08
Finish Weight (kg)	81043	2612.82
Scrap/Off-cuts weight (kg)	12323	397.29

### 3.4.2 Cost rates for embodied carbon dioxide

Total embodied energy of off-cuts = 397.29 GJ

$$= 397.29 \times 0.24 \text{ ton}$$

$$= 95.35 \text{ ton}$$

Environmental cost of the emission of one ton of CO<sub>2</sub> in 2022 = 194.28 euros

Total environment cost of the emission of CO<sub>2</sub> = 95.35 x 194.28

$$= 18524.68 \text{ euros}$$

### 3.5 Comparative analysis

Table 11 presents a comparison of the output for four different design types. From this comparison, it is observed that the highest rebar usage occurs in 4-C-16, followed by 3-C-12, 3-C-9, and 3-C-7, as the built-up area of 4-C-16 is the largest. The total cutting waste, including offcuts and scrap, is found to be the highest (15.21%) in 4-C-16. This is attributed to the use of 25 mm and 20 mm bars in the columns, as required by structural specifications, where stricter restrictions on lapping are imposed. The variation in rebar diameters across different floors and the limited space for lap splice positioning result in restricted lengths of 25 mm and 20 mm bars in columns, leading to longer offcuts in higher-diameter bars. If these offcuts cannot be utilized elsewhere, they are considered waste.

From the bar bending schedule for the 4-C-16 design type, it is identified that offcuts measuring 5040 mm in length, totaling 112 in number, are generated and remain unused, leading to the highest wastage of 25 mm bars. Similarly, offcuts measuring 5720 mm in length (104 in number) and 4810 mm in length (136 in number) are generated in 20 mm bars, contributing to significant wastage in column reinforcement. A similar pattern is observed in 3-C-7, where the cutting waste amounts to 12.49%. This design type is also a four-story building, incorporating 20 mm and 25 mm bars in its columns, further contributing to material wastage.

Similarly, both 3-C-9 and 3-C-12 are three-story buildings, with cutting waste observed at 13.43% and 11.52%, respectively. The higher ratio of wastage in 3-C-9 is attributed to design detailing in columns and beams. Based on the bar bending schedule, the percentage of offcuts in 20 mm bars is recorded as 52.30% in 3-C-9 and 36.5% in 3-C-12. As a result, the total wastage in 3-C-9 is nearly equivalent to that in 3-C-12, despite the built-up area of 3-C-12 being larger than that of 3-C-9.

The embodied energy and total environmental cost associated with rebar cutting waste are presented in the Table 11. The maximum environmental cost, calculated at €18,524, is obtained for 4-C-16. These values hold significant implications for project costs, particularly when such design types are constructed in large numbers by the government.



**Table 11:** Rebar usage, wastage, and embodied energy of type designs.

Type designs	3-C-12	3-C-9	3-C-7	4-C-16
Built-up area (sq.m)	824.4	648.12	556.51	1145.94
Typical floor plan	4 rooms	3 rooms	2 rooms	4 rooms
No. of storey	3	3	4	4
Building height (m)	13.55	13.55	13.55	16.55
Rebar usage (kg)	61346	49970	40748	81043
Cutting waste(kg)	7069	6711	5090	12323
Cutting waste (%)	11.52	13.43	12.49	15.21
Embodied energy of cutting waste (GJ)	227.9	216.36	164.1	397.29
Total environmental cost of emission of CO <sub>2</sub> due to cutting waste(euros/sq.m)	12.89	15.56	13.74	16.16

### 3.6 Data validation

From the findings the minimum and maximum rebar wastage are 11.52% and 15.21% respectively. From the literature it is known that the average rebar waste for educational buildings in Hong Kong is 9.01% (Shen & Tam, 2002) which suggest that the findings from this study is valid as the construction practice, design codes vary according to countries.

### 4. Conclusions

The assessment of structural rebar wastage reveals that key factors contributing to cutting waste include project size, design parameters (such as rebar size, lapping position, lap length, hook length, and floor height), and the level of awareness regarding bar bending schedules among designers. On-site, the most common sources of waste are design errors, poor handling and storage practices, substandard workmanship, residual cut-offs, and technical inaccuracies. Effective management of complex rebar work is essential to reduce wastage, as significant amounts of rebar can be saved through increased productivity. This can be achieved by aligning purchase orders, manufacturing, and installation processes with construction schedules and by preparing precise bar bending schedules to determine rebar details and optimal quantities. Government-implemented type designs (e.g., 3-C-12, 3-C-9, 3-C-7, and 4-C-16), used in constructing over 100 schools after the earthquake, could serve as exemplary cases. These efforts primarily emphasized structural stability through norms, codes, and policies. However, a critical gap remains in sustainable construction, energy conservation, and construction and demolition (C&D) waste management. Therefore, this research highlights the importance of assessing cutting waste to identify and implement reduction measures, as this is the most effective approach to achieving sustainable construction practices and efficient waste management.

### Declaration of conflict of interest

The authors declare that there is no financial, professional, or personal conflict of interest that could influence the work reported in this paper.

## References

- Danatzko, . J. M. & Sezen, M. ASCE, . H., 2011. Sustainable Structural Design Methodologies. *Practice Periodical on Structural Design and Construction*, 16(4).
- Khondoker, M. T. H., 2021. Automated reinforcement trim waste optimization in RC frame structures using building information modeling and mixed-integer linear programming. *Automation in Construction*, Volume 124.
- Kwon, . K., Kim, D. & Kim, S., 2021. Cutting Waste Minimization of Rebar for Sustainable Structural Work: A Systematic Literature Review. *Sustainability*, 13(11).
- Lee, D., Son, S., Kim, D. & Kim, S., 2020. Special-Length-Priority Algorithm to Minimize Reinforcing Bar-Cutting Waste for Sustainable Construction. *Sustainability*, 12(15).
- Rode, P., Burdett, . R. & Soares, J. C., 2013. Buildings: investing in energy and resource. In: *Towards a green economy: pathways to sustainable development and poverty eradication*. s.l.:United Nations Environment Programme, pp. 331-373.
- IS 13920:1993, n.d. *Indian Standard Code of Practice for Ductile Detailing of Reinforced Concrete Structures Subjected to Seismic Forces*, s.l.: Bureau of Indian Standards.
- LY, S. & Tam, V. . W., 2002. *Subcontracting arrangements and solid waste generation in the construction industry*. s.l., s.n.
- Matviyishyn, Y. & Janiak, T., 2019. *Minimization of steel waste during manufacture of reinforced concrete structures*. s.l., AIP Publishing..
- Nadoushani, Z. . S. M., Hammad, A. W. & Akbarnezhad, . A., 2016. *A Framework for Optimizing Lap Splice Positions within Concrete Elements to Minimize Cutting Waste of Steel Bars*. s.l., IAARC Publications.
- National planning commission, Government of Nepal, 2015. *Nepal Earthquake 2015: Post Disaster Needs Assessment*, s.l.: s.n.
- Poon, C. S., Yu, A. T. W. & Jaillon, . L., 2004. Reducing building waste at construction sites in Hong Kong. *Construction Management and Economics*, 22(5), pp. 461-470.
- Porwal, A. & Hewage, K. N., 2012. Building Information Modeling–Based Analysis to Minimize Waste Rate of Structural Reinforcement. *Journal of Construction Engineering and Management*, 138(8).
- Praseeda, K., Reddy, B. V. & Mani, M., 2014. Embodied energy assessment of building materials in India using process and input–output analysis. *Energy and Buildings*, pp. 677-686.
- Shen, . L. & Tam, W., 2002. *Subcontracting Arrangements and Solid Waste Generation in the Construction Industry*. s.l., s.n., pp. 25-29.

## Compliance Status of Nepal National Building Code (NBC: 105) within Pokhara Metropolitan City

Shisab Pant<sup>a\*</sup>, Ajaya Subedi<sup>b</sup>

<sup>a</sup> Department of Applied Science and Chemical Engineering, Institute of Engineering, Pulchowk Campus, Lalitpur, Nepal

<sup>b</sup> Department of Civil Engineering, Institute of Engineering, Pulchowk Campus, Lalitpur, Nepal

\*Corresponding email: [079msccd015.shisab@pcampus.edu.np](mailto:079msccd015.shisab@pcampus.edu.np)



Pokhara Engineering College Journal (ISSN: 3021-9795), Copyright © [2025] The Author(s). Published by Pokhara Engineering College, distributed under the terms of the Creative Commons Attribution 4.0 International License (CC BY-NC 4.0).

Received: 29-November-2024; Revised: 22-January-2025; Accepted: 24-January-2025

### Abstract

Earthquake-induced structural failures globally emphasize the critical need for stringent building code compliance, particularly in seismically active regions like Nepal. This research evaluates the compliance status of Nepal National Building Code (NBC 105) in Pokhara Metropolitan City (PMC), following its 2022 revision post-Gorkha Earthquake (2015). Being Nepal's second-largest urban center with seismic zoning factor ( $Z$ ) of 0.3 which is moderate in context of Nepal and have not experienced any major earthquake in recent decades, the study was necessary in the project area. The study aims to assess compliance during design and construction phases, identify barriers, and propose actionable solutions. A mixed-methods approach encompassing desk reviews, field surveys, and key informant interviews with 45 stakeholders was employed over nine months. Results revealed a meager 2.63% compliance during the design phase. These deficiencies compromise the seismic resilience of the 100,000+ buildings already constructed in PMC, raising significant safety concerns. The findings highlight that limited stakeholder awareness, insufficient technical training, economic constraints, and weak enforcement mechanisms are the primary barriers to adherence. Key recommendations include simplifying NBC provisions to enhance cost-effectiveness, implementing targeted capacity-building programs for engineers and contractors, and conducting public awareness campaigns to promote seismic safety. Additionally, retrofitting non-compliant structures and leveraging technology, such as Building Information Modeling (BIM) and remote sensing, for construction monitoring are vital steps forward. This study underscores the need for robust policy enforcement and strategic interventions to ensure seismic resilience in Nepal's urban development. By aligning safety with economic feasibility, these insights contribute to a sustainable and earthquake-resilient future.

**Keywords:** Building code compliance, NBC 105, seismic resilience, urban development

### 1. Introduction

Earthquakes, caused by abrupt movement between tectonic plates along fault lines, are among the most destructive natural disasters. Their impacts include ground shaking, soil liquefaction, landslides, avalanches, and tsunamis. Between 1998 and 2017, earthquakes were responsible for over 750,000 deaths globally, accounting for more than half of all-natural disaster-related fatalities, with 125 million people affected through injuries, displacement, or homelessness (WHO, 2017). The structural failure of buildings during earthquakes is often linked to the absence of stringent building codes and inadequate enforcement mechanisms (Usman, et al.,

2022). This underscores the critical need for robust seismic design standards and their effective implementation.

Nepal, situated at the tectonic junction of the Indian and Tibetan plates, is highly susceptible to large-magnitude earthquakes. Historical records since 1255 A.D. document 18 major earthquakes, including the catastrophic 1833, 1934, 1980, 1988 and 2015 events (Chaulagain, et al., 2018). These disasters have highlighted the need for seismic-resistant infrastructure. The development of Nepal's first National Building Code (NBC) began in 1993, followed by the enactment of the Building Act (2055 B.S.) and Regulations (2056 B.S.). To date, 23 NBC codes are in practice, ranging from NBC 000 to NBC 208, with NBC 105 specifically focusing on seismic design. However, despite these advancements, compliance remains a significant challenge (DUDBC, 2020).

Pokhara Metropolitan City (PMC), Nepal's second-most populous urban area (CBS, 2021), faces rapid urbanization. Over half a million residential structures in Nepal have suffered damage due to non-compliance with building codes, inadequate training, and the prevalent use of unskilled labor (Gautam, et al., 2016). Previous studies on seismic safety in Nepal primarily focus on structural aspects during the design phase or material strength during construction but lack insights into compliance with NBC standards. Department of Urban Development and Building Construction (DUDBC) being leading government entity for the formulation, monitoring and implementation of planning norms and building codes, initiated focusing at least a major city from each province and 10 municipalities from Kathmandu as a pilot project in improving NBC compliance. A baseline survey conducted by the DUDBC in collaboration with JICA on 200 under-construction buildings in Kathmandu highlighted the compliance rate with NBC. Figure 1 from this survey indicates that compliance was highest for column size (99%) but lowest for concrete sample testing (2%), with an average compliance rate of 55%. This baseline survey shows that compliance was particularly low in beam-column joints (22%), concrete mix ratio (6%), and concrete test piece sampling (2%). As part of this project from DUDBC, NBC implementation consultant was assigned to perform the task in Pokhara Metropolitan City (PMC) of Gandaki Province as well and this study was conducted during a nine-month engagement (Kartik 2079-Ashadh 2080).

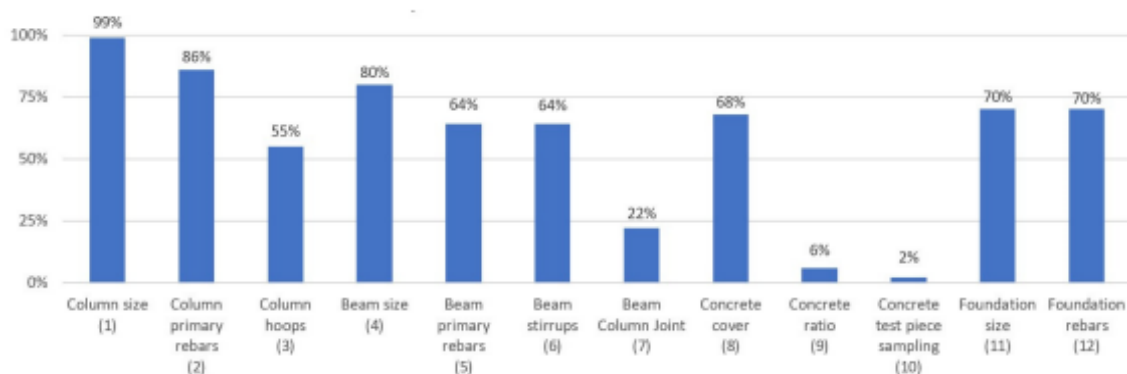


**Figure 1:** NBC compliance rate (NBCC Baseline Survey Report, 2022).

This study aims to evaluate the compliance status of NBC 105 within Pokhara Metropolitan City (PMC), focusing on both the design and construction phases. It seeks to analyze the current compliance rates, assess stakeholder familiarity with the code, and identify challenges that hinder adherence. Based on these findings, the study recommends measures to improve compliance and enhance seismic resilience. Ultimately, the insights gained are expected to

contribute to safer building practices in Pokhara and other regions, fostering a more robust approach to earthquake resistance.

## **2. Data and Methods**

### **2.1 Study Area**

Pokhara Metropolitan City, located at 28°12'30'' N and 83°59'20'' E with an elevation of approximately 822 meters in Kaski district, Gandaki, is the second most populous city in Nepal, after Kathmandu, with a population of 518,452 residing in 101,669 households (pokharamun, 2022). The city's humid sub-tropical climate, moderate temperatures, and adequate precipitation make it an ideal place to live. Since the 1990s, Pokhara has seen rapid urbanization, with service-sector industries increasingly contributing to the local economy, surpassing traditional agriculture. Additionally, the city is emerging as an education and healthcare hub for the Gandaki province.

Based on federal restructure of Nepal as per Constitution of Nepal-2072, PMC the largest metropolitan city in Nepal in terms of area covering (i.e. 464.2 k.m.<sup>2</sup>) was established initially on 10th March 2017 AD as Pokhara Lekhnath Metropolitan City and later renamed as Pokhara Metropolitan City on August 8, 2018 (pokharamun, 2022). Regarding seismic hazard, Pokhara lies in a zone with a seismic zoning factor (Z) of 0.3, considered moderate in the context of Nepal. The site's sub-soil category is typically Type B or Type C (DUDBC, 2020). While the Gorkha earthquake of 2015 severely affected cities like Kathmandu, Lalitpur, Bhaktapur, and Bharatpur, Pokhara and the western part of Nepal experienced relatively less damage. This is not due to stronger buildings, but rather the direction of seismic waves, which were transmitted eastward from the epicenter, leaving the west relatively safe. However, this seismic zone has not released significant energy for an extended period, and there is potential for seismic waves to occur at any time in the future. With over 100,000 houses already built in the area and an annual construction rate of approximately 4,000 to 5,000 houses, it is critical to ensure that both new and existing buildings are designed to withstand seismic hazards.

### **2.2 Methodology**

The technical approach and methodology were developed based on a thorough understanding of the study's scope and objectives, including anticipated challenges and their resolutions. Activities and detailed tasks were carefully formulated to ensure the achievement of the desired outputs. The research primarily employed qualitative methods, supplemented by limited quantitative data analysis. Ontological perspectives emphasized the significance of building codes in construction practices, highlighting their critical role in ensuring structural safety. Epistemologically, the study linked historical analysis, observations, and perceptions to identify issues, challenges, and opportunities in building code compliance. Axiologically, the researcher's values and beliefs underpinned a systematic, unbiased approach to constructing a clear understanding and generating scientific knowledge for effective code implementation. Methodologically, a combination of inductive and deductive reasoning within a qualitative framework was employed. This critical-interpretative-constructive paradigm ensured the alignment of research methods with the study's objectives (Joshi & Pokharel, 2022). The following approach and methodology were adopted to achieve the main objective and scope of work.



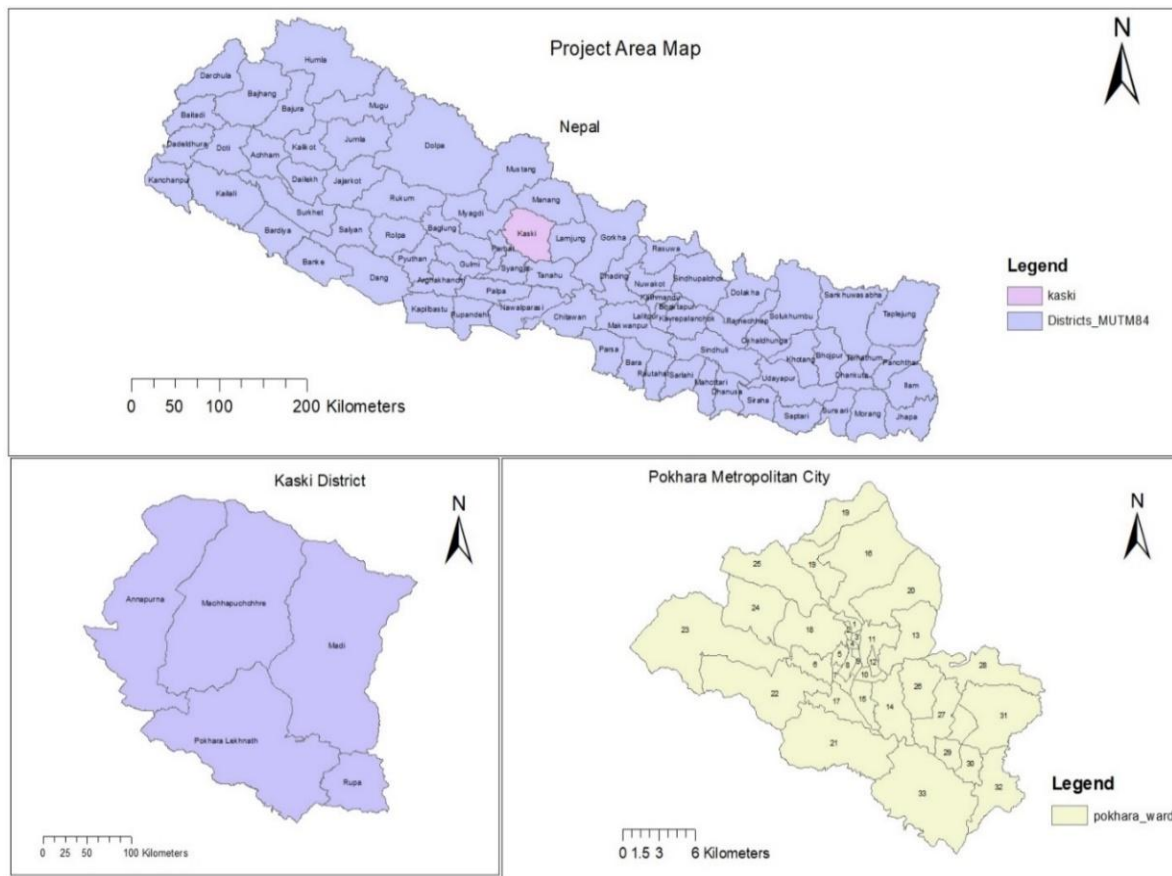


Figure 2: Study Area Map (Created using Arc-GIS).

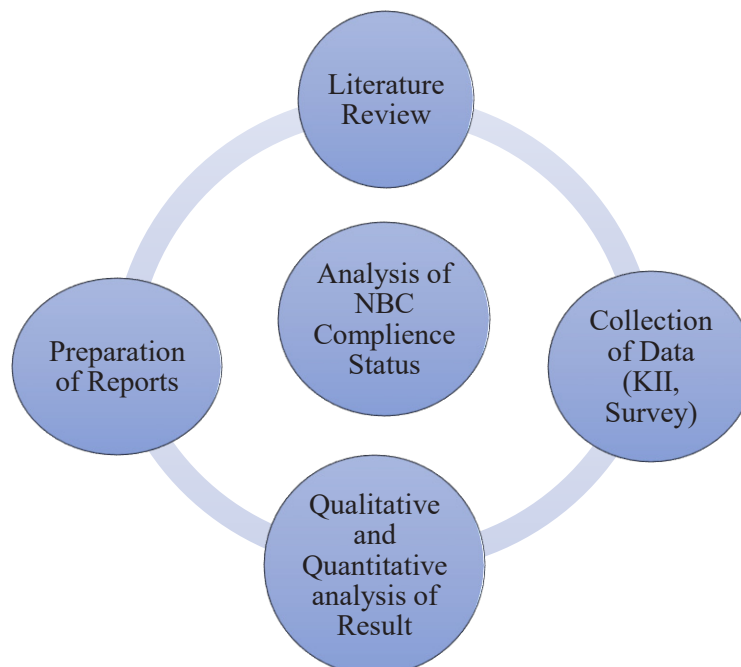


Figure 3: Flowchart of Methodology.

### 2.2.1 Desk studies

During the study, the original, firsthand data from direct survey or question for this specific objective were collected as primary data along with the already published or collected and cleaned data as secondary data. The primary data including KII to the municipality officials, baseline study etc. were also collected. Secondary data were collected in the form of reports, articles, profiles, and maps to understand the study area, site location, and geological and environmental conditions. Relevant reports on past projects and policies were reviewed alongside existing legislation, regulations, and standards applicable in Nepal, including norms, specifications, guidelines, and codes. Key documents reviewed included municipal profiles, maps, national acts and regulations related to buildings, building codes, and national plans and policies. This comprehensive desk study provided the foundational knowledge necessary for evaluating NBC 105 compliance within the study area.

### 2.2.2 Survey/KII and Discussion with municipal authorities

Data for the study was collected through a combination of municipal records, ward office visits, and stakeholder engagement. Municipal authorities, as key stakeholders, provided official data and valuable insights into the study area's current state. Information on buildings with a plinth area greater than 1,000 square feet was extracted from the Electronic Building Permit System (EBPS) of the Metropolitan City Office, while data for smaller buildings with a plinth area less than 1,000 square feet were obtained during visits to all 33 ward offices. Key Informant Interviews (KIIs) were conducted with a total of 45 stakeholders, including one representative (Engineer, Sub-Engineer, or Ward Secretary) from each ward office and 5 officials from the Metropolitan City Office, such as the Chief Administrative Officer (CAO), the heads of the Urban Development and Infrastructure Division and Building Permit Section, the Administrative Officer of the Building Permit Section, and the IT Officer followed by 7 representative from consulting firm, designers and contractors. Checklists were developed based on the literature review and study objectives to guide data collection and discussions. These checklists covered aspects such as the base codes followed in building designs, the frequency of site visits by technical personnel, common faulty practices observed, and reasons for complexities in NBC non-compliance, public awareness campaigns, and suggestions for improvement. Building code compliance during construction was assessed using data from municipal and ward-level technical personnel, supervision consultants, direct site visits, and prior studies. Critical parameters influencing structural strength, such as beam and column size, concrete mix ratio and techniques, rebar size and bending, beam-column joints, lapping and hooks, foundation size and type, curing time, and methods, were systematically analyzed. This comprehensive approach ensured the inclusion of diverse perspectives and reliable insights into building code compliance in Pokhara Metropolitan City.

## 3. Results and Discussion

### 3.1 Present Status of Building Permit Process

Pokhara, as one of the pioneering cities in Nepal, has implemented the building permit process since 2036 B.S. The Pokhara Metropolitan City (PMC) has established the Earthquake Safety and Building Permit unit within the Urban Development and Building Construction Division, consisting of 17 staff members, as shown in Table 1.



**Table 1:** Manpower details of building permit unit in metropolitan office.

Currently working Manpower	Number	Remarks
Senior Engineer	1	Unit head
Engineer	4	7 <sup>th</sup> level
Sub- Engineer	5	7 <sup>th</sup> level
Assistant sub-Engineer	1	7 <sup>th</sup> level
Administrative officer	1	7 <sup>th</sup> level
Administrative Assistant	3	4 <sup>th</sup> level
Helper	2	

*Source: PMC Building Permit Section, 2079*

The Earthquake Safety and Building Permit unit is present in all 33 wards of the city, each with a team authorized to issue permits for simple group 'C' buildings (i.e., buildings with a plinth area < 1000 sq. ft.). Table 2 summarizes the manpower allocation across these wards. Since 2073 B.S., the Electronic Building Permit System (EBPS) has been implemented. This system maintains records of building permits, including temporary and permanent permits, completion certificates, ownership details, land certificates, and engineering drawings, all in digital format. Although the system is effective, there is an ongoing need for more advanced management and storage software, with digitization efforts starting in fiscal year 2079/080.

**Table 2:** Manpower details of building permit unit in different ward office.

Currently working manpower	Number	Remarks
Engineer	1	In all 33 wards
Sub- Engineer	1 or 2	In all 33 wards
Administrative officer	1	In all 33 wards
Administrative Assistant	1	In all 33 wards
Amin	1	In all 33 wards

*Source: Building Permit Section of PMC, 2079*

### 3.2 Building Permit and Construction Completion Rate in Last Few Years

An analysis of the provided data from the PMC and various ward offices reveals a significant decline in building construction during the Covid pandemic. Before the pandemic, approximately 5,000 houses were constructed annually, but this number has decreased to around 2,000-3,000 houses per year (PMC, 2021). Despite this, the urbanization rate in Pokhara remains high, and the building permit process is smooth, with the construction completion rate nearly equal to the number of temporary permits issued, suggesting efficient and timely services. The recent building construction registration and completion trend also suggest the rate of type c building i.e. plinth area <1000 Sq. ft. are increasing whereas the type A and B building's are continuously goes on decreasing which may be due to financial crisis after the covid and the subconscious fear of Gorkha earthquake-2015.

### 3.3 Implementation of NBC: 105 in Building Permit Process

Buildings taller than 17 meters or those with more than five stories are classified as high-rise buildings (PMC, 2075). These buildings must adhere to NBC 105 regulations for design. Other buildings follow NBC guidelines for architecture, but use IS codes for seismic design, as outlined in Table 3.

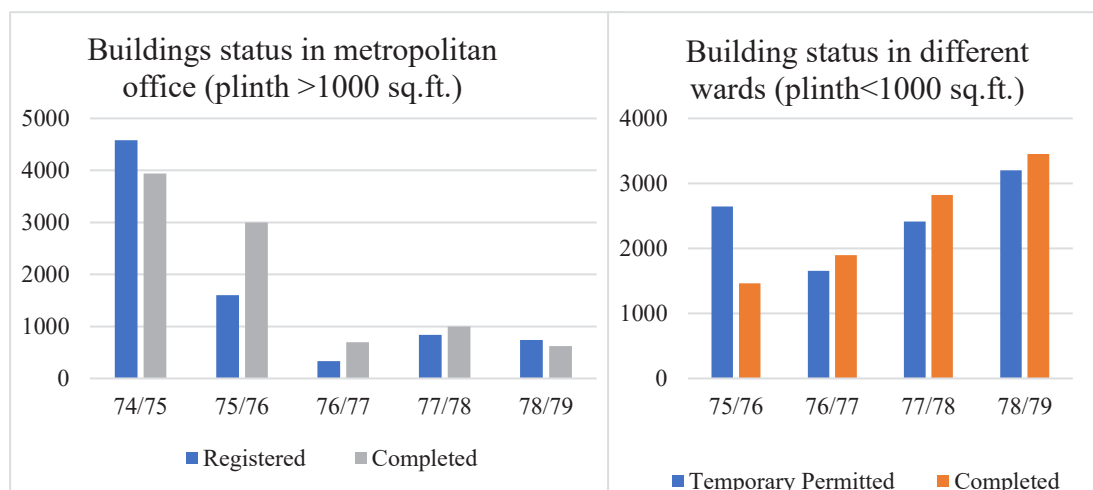


**Figure 4:** Building Permit Details of Building from Metropolitan City Office and Ward Offices (i- Category A and B, ii- Category C).

**Table 3:** Type of Codes followed in different Building Design.

S.N.	Type of building	Permission from	Code followed in design
1	Small building having plinth area <1000 sq. ft. (MRT)	Ward office	NBC (101,201,205,202)
2	Any type of building having plinth area >1000 sq. ft.	Metropolitan office	All NBC codes and IS codes (for seismic design)
3	High rise building (Ht. > 17m. or 5 storey)	Metropolitan office after approval of technical committee	All NBC codes

Data from the fiscal year 2078/079 as per building permit section's record in PMC reveals that only 2.63% of buildings followed NBC 105:2020, while 15.6% adhered to IS codes, and the remaining 81.76% followed MRT standards. The primary reasons for the low compliance with NBC 105 include lack of public awareness about seismic hazards and the economic benefits of

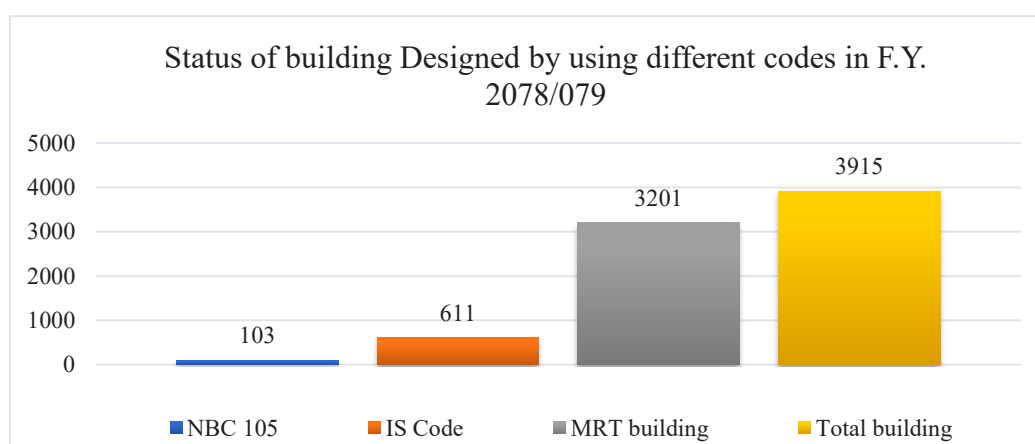


**Figure 5:** NBC and other codes compliance status.

IS designs, as noted in clauses 4.2.1 and 4.4.2 of NBC 105 (2020), which require larger cross-section for structural elements. Proper seismic design alone does not ensure structural safety during an earthquake. Quality materials and skilled labor are critical, as is continuous

supervision throughout construction. Although high-rise buildings in PMC follow NBC 105, construction and supervision of such buildings have been suboptimal.

In PMC, a similar to Kathmandu trend as shown in Figure 1 was observed during site visits and compliance checks. Based on the answer from technical person within the metropolitan city who had carried out the construction supervision and site verification, the construction time compliance has ranked on the following order.

**Table 4:** Ranking of Construction time compliance.

S.N.	Parameters observed during site visit	Rank based on issues in compliance
1	Sample Testing	1
2	Concrete mix ratio	2
3	Beam-Column joint	3
4	Stirrups hook/bending and rebar's spacing	4
5	Clear cover	5

Construction time compliance was mainly analyzed based on the answer related to site visit experience of municipal technical persons and few building construction sites visited by the researcher. Low NBC compliance during construction is largely attributed to insufficient training for municipal engineers, designers, contractors, and masons, compounded by poor supervision from consultants and municipality engineers. Dedicated technical manpower for the building supervision in the municipality, technical skill development training, use of remote sensing technology for the continuous monitoring during construction phase and advance building information modeling (BIM) integrated EBPS system could really be beneficial in the compliance of building code and enhance of seismic safety within PMC. With over 100,000 buildings already constructed in PMC, there is uncertainty regarding the seismic safety of these structures when an earthquake hits Pokhara.

#### 4. Conclusions

The evaluation of compliance with Nepal National Building Code (NBC 105) in Pokhara Metropolitan City (PMC) reveals significant gaps in adherence, threatening the seismic safety of this rapidly urbanizing region. Despite PMC's pioneering efforts in implementing a building permit system since 2036 B.S., only 2.63% of buildings adhered to NBC 105 standards during the design phase. Specific areas of concern during construction phase include concrete sample testing, beam-column joint detailing, concrete mix ratio, rebars spacing and stirrups hook/bending and clear cover. These deficiencies are largely attributed to limited awareness among stakeholders, insufficient training for municipal engineers and contractors, economic disincentives due to the high cost of compliance, and inadequate supervision mechanisms. Over 100,000 buildings constructed in PMC, combined with an annual construction rate of 4,000-5,000 houses, exacerbate concerns about the region's seismic vulnerability. To address these challenges, simplifying NBC provisions for cost-effectiveness is essential, alongside capacity-building initiatives targeting municipal engineers, designers, and contractors. Internationally, it has been observed that many of the challenges related to building code compliance can be minimized through proactive measures such as training, raising awareness, and providing technical support to code users (Nwadike & Wilkinson, 2020). Additionally, leveraging technologies such as Building Information Modeling (BIM) and remote sensing for continuous construction monitoring could enhance compliance rates. Retrofitting non-compliant existing structures must be prioritized to mitigate risks. The findings of this study underscore the critical

need for robust enforcement of NBC standards and proactive measures to foster a culture of compliance. These strategies are essential not only for safeguarding life and property in PMC but also for setting a precedent in achieving seismic resilience across Nepal.

### Acknowledgements

The authors are thankful to the respected personnel who spared their valuable time for the key informant interview.

### References

- Bhandari, A., Suwal, R. & Khawas, A., 2023. *Seismic Response of Irregular High Rise Building in Kathmandu*. Lalitpur, s.n., pp. 910-916.
- CBS, 2021. CBS. [Online] Available at: <https://censusnepal.cbs.gov.np/results> [Accessed 25 December 2024].
- Chaulagain, H., Gautam, D. & Rodrigues, H., 2018. Impacts and Insights of the Gorkha Earthquake. *Elsevier*, Volume Chapter 1, pp. 1-17.
- DUDBC, 2020. *Seismic Design of Buildings in Nepal, NBC 105: 2020*. Kathmandu: Department of Urban Development and Building Construction (DUDBC).
- DUDBC, 2022. *National Building Code Compliance (NBCC) Baseline Survey*, Kathmandu: Department of Urban Planning and Building Construction (DUDBC).
- Gautam, D., Rodrigues, H., K.K. Bhetwal, P. N. & Sanada, Y., 2016. Common structural and construction deficiencies of Nepalese. *Cross Mark*.
- Joshi, J. C. & Pokharel, J. R., 2022. *Issues and Challenges in Urban Planning and Practices*. Lalitpur, 12th IOE Graduate Conference.
- Nwadike, A. N. & Wilkinson, S., 2020. Challenges facing building code compliance in New Zealand. *International Journal of Construction Management*.
- PMC, 2075. *Byelaws Related Rules of Pokhara Metropolitan City*, Pokhara, Nepal: Pokhara Metropolitan City, Local Gazette.
- pokharamun, 2022. [Online] Available at: <https://pokharamun.gov.np/> [Accessed 15 12 2022].
- Usman, Z., Asmawi, M. Z. B. & Ariffin, N. A. M., 2022. BUILDING CODES IN RURAL AREAS OF PAKISTAN. *Planning Malaysia: Journal of Malaysian Institute of Planners*, Volume Vol. 20, pp. 444-461.
- WHO, 2017. *World Health Statistics*, s.l.: World Health Organization.

## Diabetic Retinopathy Detection through Multiclass Classification of Fundus Image Using Convolutional Neural Network

Sandep Gupta<sup>1\*</sup>, Ashim Khadka<sup>2</sup>

<sup>1</sup> Department of Computer Engineering, Pokhara Engineering College, Pokhara, Nepal

<sup>2</sup> Department of Electronics and Communication Engineering, NCIT, Kathmandu, Nepal

Corresponding email: [kasaudhansandep48@gmail.com](mailto:kasaudhansandep48@gmail.com)



Pokhara Engineering College Journal (ISSN: 3021-9795), Copyright © [2025] The Author(s). Published by Pokhara Engineering College, distributed under the terms of the Creative Commons Attribution 4.0 International License (CC BY-NC 4.0).

Received: 20-November-2024; Revised: 25-January-2025; Accepted: 03-February-2025

### Abstract

Diabetic retinopathy (DR) is an eye disease which is caused by high blood sugar and high blood pressure and damage the blood vessels in the back (retina) of the eye. Diabetic retinopathy (DR) is not a reversible process and treatment only sustain vision. The number of ophthalmologists cannot meet the growing demands around the world. This study focuses on the automatic diagnosis of the disease through deep learning. Convolutional neural network (CNN) is more widely used as a deep learning method in medical image analysis. Multiclass image classification of images into non referable DR and referable DR has been done using proposed Convolutional neural network (CNN) model. For multiclass classification problem, the sensitivity, specificity and F2 score value for class 0 (no DR) are 81.75 %, 91.06 % and 81.80 % respectively. Whereas for class 1 (non-severe DR), sensitivity, specificity and F2 score values are 71.28 %, 78.52 % and 70.01 % respectively. Similarly for class 2 (sever DR), sensitivity, specificity and F2 score values are 73.03 %, 93.39 % and 75.08 % respectively. Bayesian optimization has been performed for tuning learning rate and gives optimal learning rate 0.000358 through the optimization process. The customized CNN is then trained using 0.000358 learning rate and then tested on test data. The images in dataset have poor contrast and consists of impulse noises. Contrast limited adaptive histogram equalization (CLAHE) method is used to improve the contrast of the image followed by median filter to remove noise present in DR image.

**Keywords:** DR, CNN, CLAHE, Deep Learning, Bayesian Optimization

### 1. Introduction

Diabetes is a disease that increases the amount of glucose in the blood caused by a lack of insulin (Alyoubi, Shalash and Abulkhair, 2020). Diabetes influences the eyes and vision in various ways, including visual impairment, cataract glaucoma, impact on optic nerve, temporary paralysis of the muscles on the outside of the eye, and double vision. But the most common and most important of these artifacts is the impact on the retina (Alyoubi, Shalash and Abulkhair, 2020). Diabetic Retinopathy (DR) is a complication of diabetes that causes the blood vessels of the retina to swell and to leak fluids and blood (Shanthi and Sabeenian, 2019; Torabian, Ghaderi and Kafiye, 2018). DR is one of the main causes of reduced vision and the probability of DR increases with longer duration of being affected with diabetes. People with untreated diabetes are more likely to lose their eyesight than normal people (Alyoubi, Shalash and Abulkhair, 2020). DR is a silent disease and affects up to 80 of the diabetics around the world. Every eleventh per- son in the world suffers from diabetes mellitus, a disorder of sugar

metabolism, whose prevalence is expected reach every tenth person by 2040 (Piresa et al., 2019). It is reported that approximately 1/3(34.6) of people with diabetes have DR to some extent in the U.S, Europe and Asia. It is also noted that 1 in 10 have vision-threatening DR (Li et al., 2019). The world Health Organization (WHO) and professional organization such as American Academy of ophthalmologists recommend eye examination at least once a year for DR. However poor or isolated communities often cannot afford such frequent consultants with ophthalmologists, frustrating only diagnosis treatment. Since the disease is a progressive process, medical experts suggest that diabetic patient need to be detected not less than twice a year in order for DR. However, the early screening of DR remains a challenge for several reasons. First diabetes is generally treated at endocrinology department in hospitals and fundus examination has long been ignored resulting in delayed treatment for many patients. Second, the process of DR screening is time consuming. Consequently, only a certain number of patients can be processed each day. Third, the number of ophthalmologists cannot meet the growing demands around the world (Li et al., 2019).

Automated DR screening through deep learning is an alternative solution to the above problems, with the advantages of high efficiency, low cost and minimal dependencies on clinicians. Deep learning method has been widely used in image analysis process. It can be used for medical image analysis process and can help in clinical diagnosis. Unlike conventional machine learning methods that rely heavily on feature engineering, deep learning algorithms automatically learn the most predictive representations in a manner of layer-by-layer combination. CNN are one of the important methods of deep learning in which several layers are trained with a powerful method. This method is very efficient and it is one of the most common methods in the various application of computer vision. CNN consist of convolution layers, max or average pooling layers and fully connected layers as main layers.

Figure 1 shows the fundus images for normal retina and DR including all those lesions (Panel and Patre, 2018). There are five stages of DR depending on the presence of these lesions, namely, no DR, mild DR, moderate DR, severe non-proliferative DR and proliferative DR, which are briefly described in Table 1 No DR, mild DR, moderate DR are categorized in non-referral DR while severe DR and proliferative DR are referral DR.

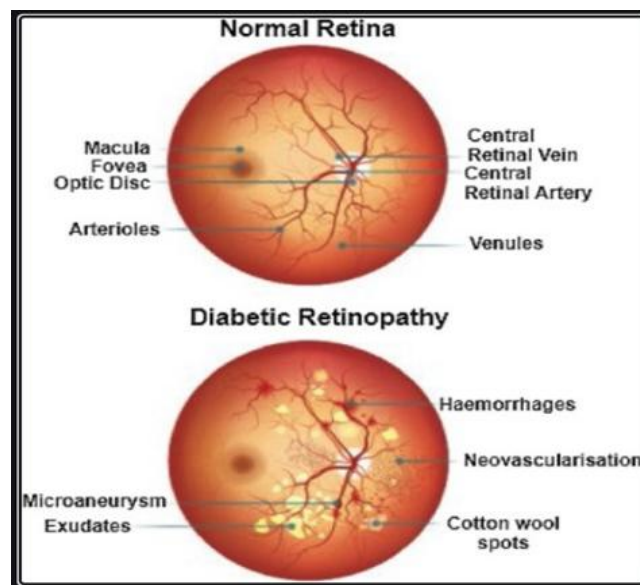


Figure 1: Difference between normal retina and diabetic retinography (Huang et al., 2017).



**Table 1:** Lists of diabetic retinopathies with its associative lesions (Alyoubi, Shalash and Abulkhair, 2020).

DR severity level	Lesions
No DR	Absent of lesions
Mild non-proliferative DR	Micro-aneurysm only
Moderate non-proliferative DR	more than just microaneurysm but less than severe DR
Severe non-proliferative DR	Any of the following <ul style="list-style-type: none"> <li>● more than 20 intra-retinal hemorrhage</li> <li>● definite venous beeding in 2 quadrants</li> <li>● Prominent intra-retinal micro-vascular abnormalities in 1 quadrant</li> <li>● no signs of proliferative DR</li> </ul>
Proliferative DR	Any of the following <ul style="list-style-type: none"> <li>● Vitreous</li> <li>● Pre-retinal haemorrhages</li> <li>● Neo-vascularization</li> </ul>

## 2. Materials and Methods

### 2.1 Objective and contribution of the research

#### 2.1.1 Objective

To detect the severity of fundus image through multiclass classification.

#### 2.1.2 Contribution of the Research

The contributions of the research are given below

- Bayesian optimization has been performed for tuning learning rate for multi-class classification. Multiclass image classification was done in order to provide more variation in the referral assessment of DR images. Such as images that belong to class 2 (severe non-proliferative DR and proliferative DR) should be referred earlier than images belonging to class 1 (mild DR and moderate DR). Whereas images that belong to class 0 are non-referable as they absence any DR lesions.
- Dataset were highly pre-processed through a series of multiple tasks to obtain good quality image. The images were cropped in order to remove unnecessary back- ground. Then CLAHE operation has been applied followed by the median filtering technique in order to improve the poor contrast of image and remove the noise present in image.
- Total image dataset was prepared using five different datasets such as IDRiD, Messidor, EYEPACS, kaggle APTOS and DDR reflecting the diversity in the image dataset.
- Customized CNN algorithm was used as a deep learning methodology.

### 2.2 Methodology

The block diagram of the proposed model is shown in Figure 2.

### 2.2.1 Data Collection

Table 2 shows the number of images taken for the multiclass classification. Class 0 (no DR) includes 4, 676 images, class 1 (mild DR and moderate DR) includes 8, 658 images and class 2 (severe non-proliferative DR and proliferative DR) includes 5, 686 images.

**Table 2:** Total Number of image data for multiclass classification.

No DR image	Non-Severe DR image	Severe DR image	Total Number of DR image
4,676	8,658	5,686	19,020

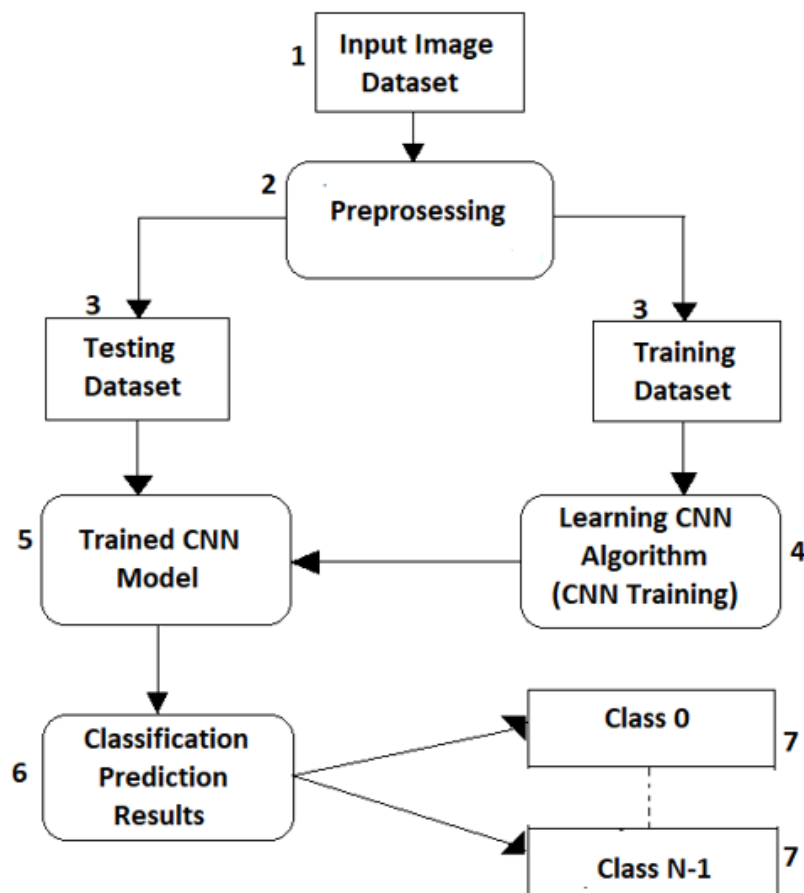


**Figure 2:** Block diagram of proposed model.

### 2.2.2 Preprocessing

The aim of preprocessing is to increase the quality of an image by reducing the amount of noise appearing in the image and highlighting features that are used in image classification. Figure 3 shows the series of tasks which are carried out for preprocessing the fundus image dataset to improve the quality of the image. Retinal images are normally affected with impulse noise during image acquisition. Noise detection and removal is an important process as the image are corrupted by impulse noise because of transmission and acquisition. Also, non-uniform illumination and poor contrast due to the anatomy of fundus image, opaque media, and wide-angle optics of the camera, insufficient pupil size, sensing array geometry, and the movement of the eye are the major causes of the low-quality retinal images. The signs of DR are micro-aneurysm, hemorrhages, edema, hard exudates and cotton wool spots. The exterior of those DR

lesions varies. For example, microaneurysm and hemorrhages are red dark spots and are mostly undividable from the background while exudates are a high contrast yellow color. The accuracy of all these symptoms(lesions) depends on the quality of acquired retinal image. Before the detection of abnormalities and feature selection in retinal images, it is must to remove the different noise present in the retina, which will automatically increase the quality of the image. Therefore, the use of good quality retinal images is very essential for accurate detection, diagnosis and damage assessment of retina.

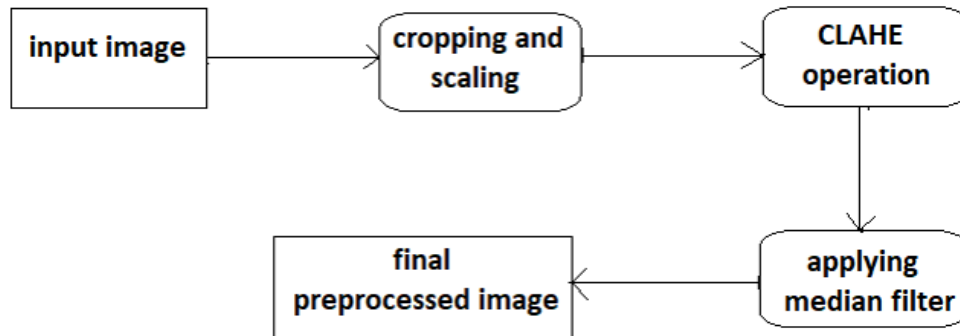


**Figure 3:** Preprocessing of Fundus Image.

### 2.2.3 CNN algorithm

The architecture being utilized is shown in figure 4 This methodology is utilizing a 21 layered approach with each layer having its own specification. Algorithm consists of feature extracting layers and classification layers. Five sets of convolution layer have been used as feature extracting layer. In each set two convolution layers having same number of filter and same kernel size has been used. The number of filters for convolution layers goes on increasing as we move deeper into the network. Given the input image, first convolution layer convolves 32 different kernel of size  $3 \times 3$  to extract low level features from the input image like edges. Also, the image is zero padded along each size of image by 1. Convolution layer uses the ReLU activation function to produce nonlinear output feature map. Convolution layer is followed by the batch normalization. The use of batch normalization is important in deep learning. Training deep neural network with tens of layers is challenging as they can be sensitive to the initial random weights and configuration of the learning algorithm. This problem is known as internal covariate shift. Batch normalization solves this major problem of internal covariate shift. It is a technique for training very deep neural networks that normalizes the contribution to a layer for every mini-batch. This has the impact of settling the learning process and drastically decreasing the number of training epochs required to train deep neural networks.

Second convolution layers also have the same kernel size of 32 but is followed by the batch normalization and max pooling layer of kernel size  $3 \times 3$  with strides 2. This combination of convolution + batch normalization + convolution + batch normalization+ max pooling is repeated for the entire feature extracting layers. One dimensional flattening of the CNN is accomplished by the Global average pooling layer followed by the 5 fully connected layers (1024, 256, 64, 32 and 8) which helps to identify very small lesion like micro-aneurysm, hemorrhages. The classification output is predicted using SoftMax activation function and dropout is performed after each dense layer to reduce the chances of overfitting.

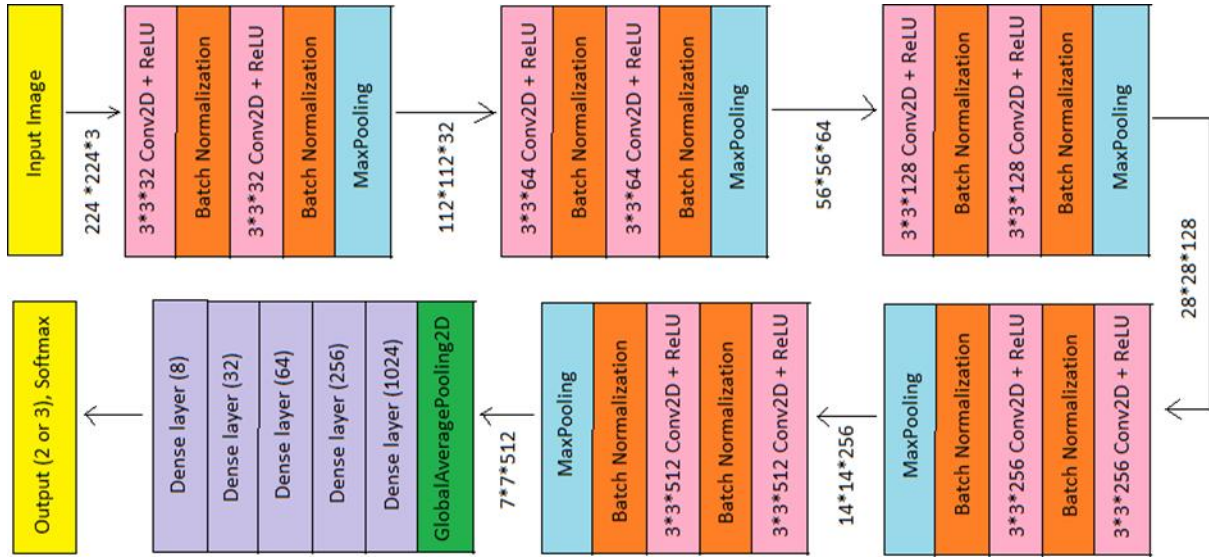


Figure 4: Structure of CNN model.

### 3. Results and Discussion

10-fold cross validation has been used for hyperparameter tuning purpose. Learning rate and train-test split ratio of dataset are the hyper-parameters which are tuned through 10-fold cross validation for the proposed model. Table 3 shows the results of 10-fold cross validation for different training-testing split ratio using different learning rate from 0.0001 to 0.001 with increment of 0.0001. Optimal result is obtained for 70:30 training- testing split ratio when learning rate is 0.0004.

**Table 3:** Testing accuracy for different learning rate with different split ratio.

Learning rate	80: 20	70: 30	60: 40	50: 50
0.0001	0.6300	0.6000	0.6000	0.5900
0.0002	0.7590	0.7610	0.7600	0.7420
0.0003	0.7630	0.7680	0.7520	0.7270
0.0004	0.7820	<b>0.7880</b>	0.7340	0.7130
0.0005	0.7010	0.7090	0.6800	0.6600
0.0006	0.7420	0.7430	0.7030	0.7010
0.0007	0.7710	0.7740	0.7500	0.7320
0.0008	0.7620	0.7640	0.7360	0.7220
0.0009	0.7170	0.7180	0.6980	0.6690
0.001	0.7120	0.7050	0.6940	0.6730

Hence the proposed CNN model is trained with optimal hyperparameter set i.e. learning rate of 0.0004 and 70:30 train-test split ratio. Table 4 shows the performance result of the model for multiclass image classification problems. Sensitivity, specificity and F2 score value for level 0 are 81.75%, 91.06% and 81.8% respectively. For level 1, sensitivity, specificity and F2 score value are 71.28%, 78.52% and 70.01% respectively. Similarly for level 3, sensitivity, specificity and F2 score value are 73.03%, 93.39% and 75.08%. Figure 5 shows the confusion metrics and ROC curve for the multiclass classification problems. All the classification curves are near to 1 value of ROC curve. Figure 6 shows the accuracy and loss curve for multiclass

classification problem. It can be observed that testing accuracy and loss curve converge and follows the training accuracy and loss curve which indicates the good fitting of the model.

**Table 4:** Score table for Multiclass classification.

Class level	Sensitivity	Specificity	F2 score
Level 0	0.8175	0.9106	0.8180
Level 1	0.7128	0.7852	0.7001
Level 2	0.7303	0.9339	0.7508

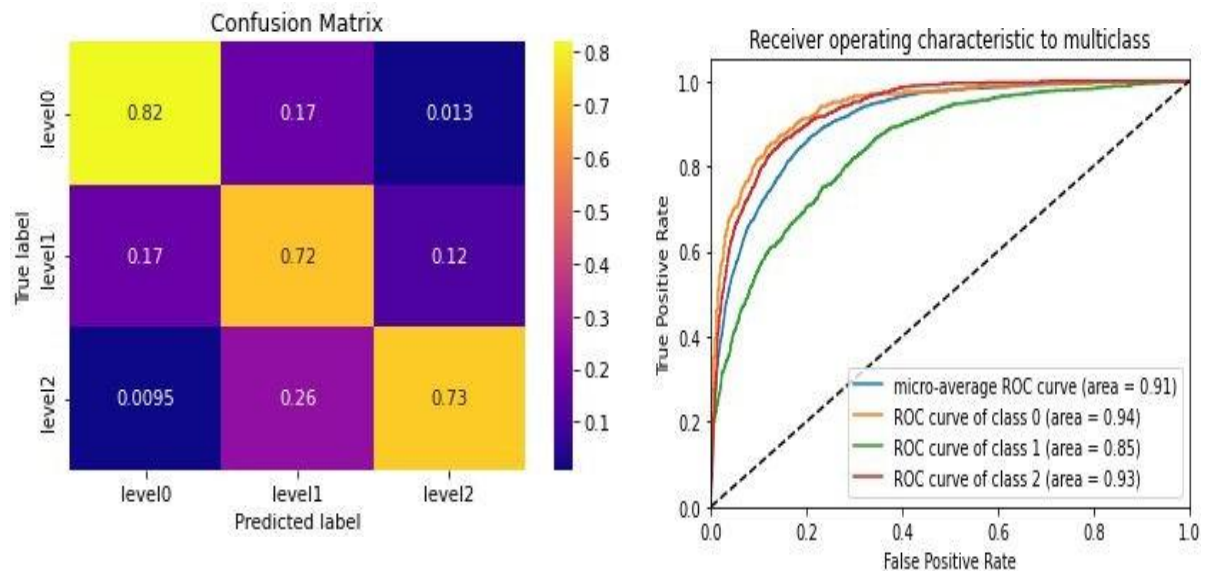


**Figure 5:** Confusion metrics and ROC curve for learning rate 0.0004 and batch size 32.

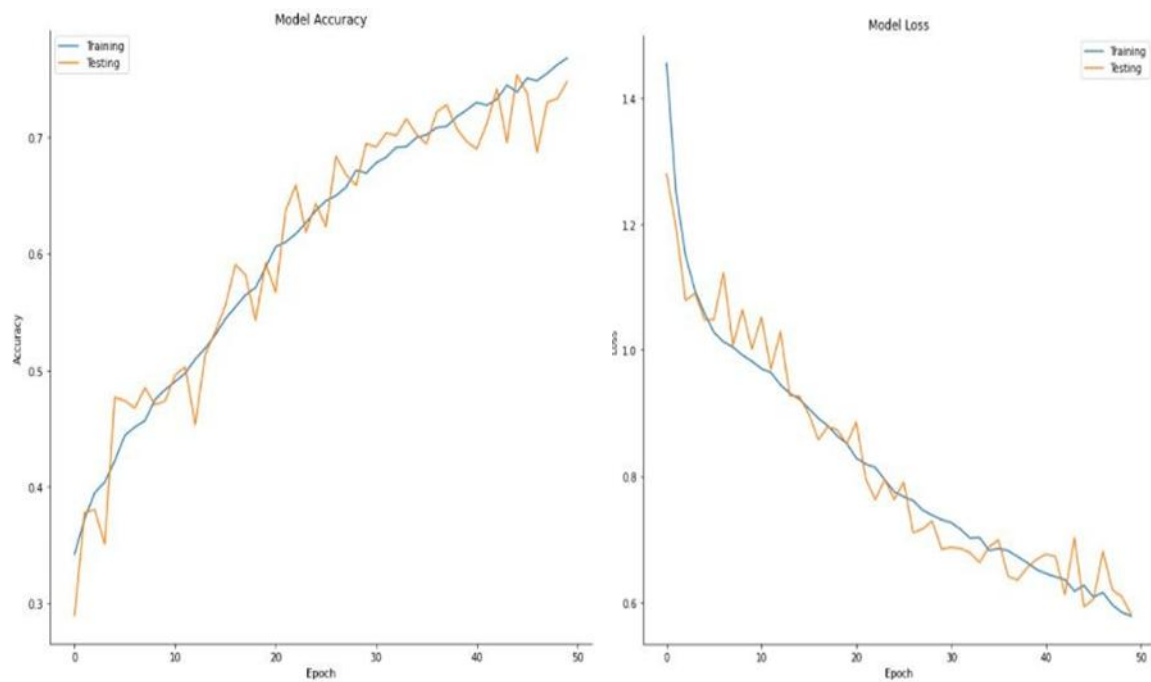


**Figure 6:** Accuracy and Loss Curve for multiclass classification.

### 3.1 Bayesian Optimization

Bayesian optimization takes into account past evaluations when choosing the hyperparameter set to evaluate next. By choosing its parameter combination in an inferred way, it enables itself to focus on the area of the parameter space that it behaves will bring the most promising validation scores. Bayesian optimization has been performed for tuning learning rate for multi-class classification and gives optimal learning rate 0.000358 through the optimization process. The customized CNN is then trained using 0.000358 learning rate and then tested on test data. Table below shows the score table for multiclass classification with learning rate tuned through Bayesian optimization. The sensitivity, specificity and F2 score value for class level 0 are 83.66 %, 91.54 % and 83.54 % respectively. For class level 1, sensitivity, specificity and F2 score values are 78 %, 84.93% and 76.77 % respectively. Similarly for class level 2, sensitivity, specificity and F2 score values are 76.07 %, 92.36 % and 77.41 % respectively as shown in table 5. Figure 7 shows the confusion metrics and roc curve for multiclass classification whereas figure 8 below shows the accuracy and loss curve. It can be observed that testing accuracy and loss curve converge and follows the training and loss curve which is better than that of former multiclass classification without using Bayesian optimization algorithm.

**Table 5:** Score table for multiclass classification, learning rate 0.000358.

Class Level	Sensitivity	Specificity	F2 score
Level 0	0.8366	0.9154	0.8354
Level 1	0.7800	0.8493	0.7677
Level 2	0.7607	0.9236	0.7741

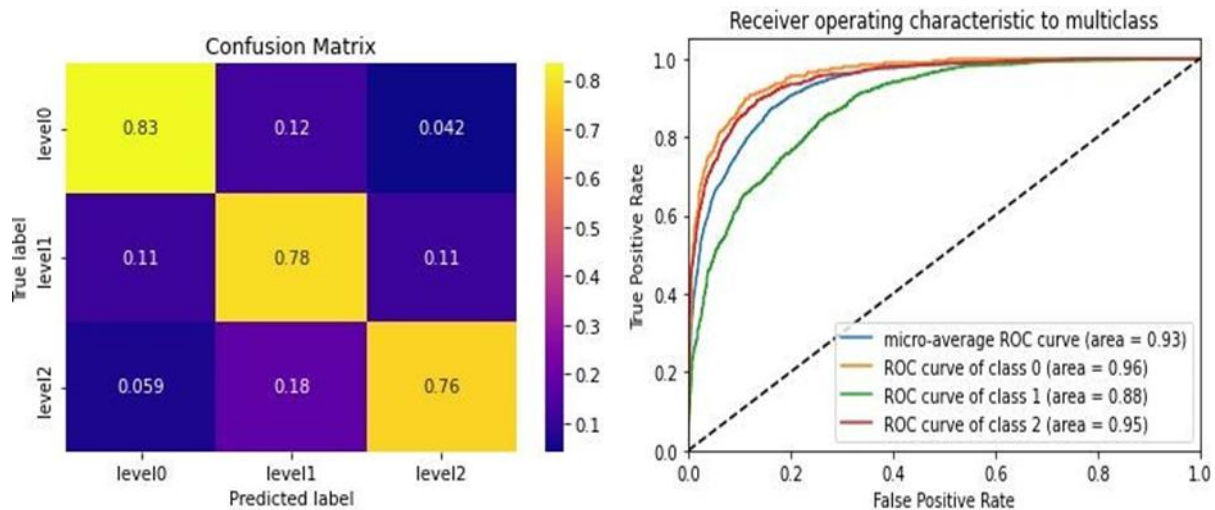


**Figure 7:** Confusion metrics and ROC curve for learning rate: 0.000358.



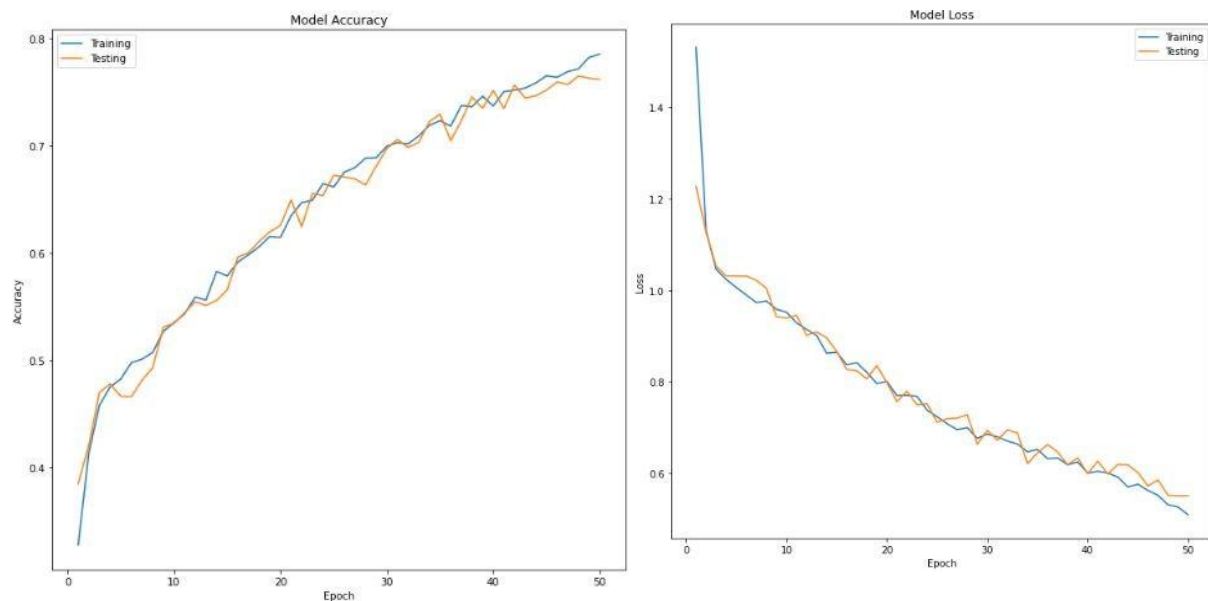


**Figure 8:** Accuracy and loss curve for learning rate: 0.000358.

#### 4. Conclusions

Multiclass classification of DR images was done into class level 0 (no DR), class level 1 (mild DR and moderate DR) and class level 2 (severe non proliferative DR and severe proliferative DR) using the proposed CNN model. 10-fold cross validation was done in order to get the optimal learning rate and train-test split ratio which are 0.0004 and 70: 30 respectively. Sensitivity, specificity and F2 score value for level 0 are 81.75%, 91.06% and 81.8% respectively. For level 1, sensitivity, specificity and F2 score value are 71.28%, 78.52% and 70.01% respectively. Similarly for level 3, sensitivity, specificity and F2 score value are 73.03%, 93.39% and 75.08%. Bayesian optimization has been performed for tuning learning rate for multi-class classification and gives optimal learning rate 0.000358 through the optimization process.

#### Acknowledgements

I would like to acknowledge and give my warmest thanks to Ashim Khadka, PhD who made this work possible. His guidance and advice carried me through all the stages of writing my research.

#### References

- Alyoubi, W.L., Shalash, W.M. and Abulkhair, M.F. (2020) 'Diabetic retinopathy detection through deep learning techniques: A review', *Informatics in Medicine Unlocked*, 20, 100377. Available at: <https://doi.org/10.1016/j.imu.2020.100377> (Accessed: 13 February 2025).
- Huang, G. et al. (2017) 'Densely Connected Convolutional Networks', *2017 IEEE Conference on Computer Vision and Pattern Recognition (CVPR)*, pp. 2261–2269. Available at: <https://doi.org/10.1109/CVPR.2017.243> (Accessed: 13 February 2025).
- Li, T. et al. (2019) 'Diagnostic assessment of deep learning algorithms for diabetic retinopathy screening', *Information Sciences*, 501, pp. 511–522. Available at: <https://doi.org/10.1016/j.ins.2019.06.001> (Accessed: 13 February 2025).

Panel, R. and Patre, B. (2018) ‘Algorithms for red lesion detection in Diabetic Retinopathy: A review’, *Biomedicine and Pharmacotherapy*, 107, pp. 681-688. Available at: <https://doi.org/10.1016/j.biopha.2018.08.111> (Accessed: 13 February 2025).

Piresa, R. et al. (2019) ‘A data-driven approach to referable diabetic retinopathy detection’, *Artificial Intelligence In Medicine*, 96, pp. 93–106. Available at: <https://doi.org/10.1016/j.artmed.2019.03.005> (Accessed: 13 February 2025).

Shanthi, T. and Sabeenian, R.S. (2019) ‘Modified Alexnet architecture for classification of diabetic retinopathy images’, *Computers and Electrical Engineering*, 76, pp. 56–64. Available at: <https://doi.org/10.1016/j.compeleceng.2019.03.017> (Accessed: 13 February 2025).

Torabian, M., Ghaderi, M. and Kafiyeh, R. (2018) ‘Classification of diabetic and normal fundus images using new deep learning method’, *Leonardo Electronic Journal of Practices and Technologies*, ISSN 1583-1078.



## **Pokhara Engineering College (PEC)**

Phirke, Pokhara-8, Kaski, Nepal

PO Box: 540, Tel: 977-61-581209/578530

E-mail: [info@pec.edu.np](mailto:info@pec.edu.np).

[www.pec.edu.np](http://www.pec.edu.np)